Biophysical Journal Volume 108 June 2015 2794–2806

Article

Direct Cytoskeleton Forces Cause Membrane Softening in Red Blood Cells

Ruddi Rodríguez-García,[1] Iván López-Montero,[1,2] Michael Mell,[1,2] Gustavo Egea,[3] Nir S. Gov,[4] and Francisco Monroy[1,2,*]

[1]Department of Physical Chemistry, Universidad Complutense. Ciudad Universitaria, Madrid, Spain; [2]Instituto de Investigación Hospital Doce de Octubre (i+12), Madrid, Spain; [3]Departament of Cell Biology, Immunology and Neurosciences, University of Barcelona School of Medicine and Institut d'Investigacions Biomèdiques August Pi i Sunyer (IDIBAPS) and Nanociències i Nanotecnologia (IN^{2}UB), Barcelona, Spain; and [4]Department of Chemical Physics, Weizmann Institute of Science, Rehovot, Israel

ABSTRACT Erythrocytes are flexible cells specialized in the systemic transport of oxygen in vertebrates. This physiological function is connected to their outstanding ability to deform in passing through narrow capillaries. In recent years, there has been an influx of experimental evidence of enhanced cell-shape fluctuations related to metabolically driven activity of the erythroid membrane skeleton. However, no direct observation of the active cytoskeleton forces has yet been reported to our knowledge. Here, we show experimental evidence of the presence of temporally correlated forces superposed over the thermal fluctuations of the erythrocyte membrane. These forces are ATP-dependent and drive enhanced flickering motions in human erythrocytes. Theoretical analyses provide support for a direct force exerted on the membrane by the cytoskeleton nodes as pulses of well-defined average duration. In addition, such metabolically regulated active forces cause global membrane softening, a mechanical attribute related to the functional erythroid deformability.

INTRODUCTION

Although it was discovered some time ago that ATP is a critical factor in the maintenance of the global shape of red blood cells (RBCs) (1–3), the metabolic regulation of red cell deformability was clearly pointed out only recently (4–7). The elastic properties of RBCs are dominated by the interaction between the lipid bilayer and the underlying spectrin cytoskeleton (8,9), which is a dynamical meshwork mainly consisting of spectrin filaments linked by reconfigurable junctional complexes (5,6). The transient binding capacity of these complexes depends on their phosphorylation state (10–12). This structural network endows the spectrin skeleton with the basic role of globally imparting structural rigidity to the cell membrane (13) and locally regulating its flexibility through reversible phosphorylation at the anchoring nodes (6,14). Indeed, the ability of RBCs to undergo reversible large deformations cannot be rationalized on the basis of a fixed connectivity of the cytoskeleton, but instead requires a model that attributes metabolically driven forces to active remodeling of the RBC cytoskeleton (6,14). Therefore, RBC dynamics has been postulated to be metabolically regulated by continuous remodeling of the junctional nodes of the spectrin skeleton (6–8,14). Under the optical microscope, normal RBCs experience large membrane undulations at the equatorial emplacement, a phenomenon originally referred to as the RBC flicker (15,16). This was initially interpreted as the manifestation of metabolic activity (17,18), although several works treated the fluctuations as purely thermal (19–21). Recently, the RBC flickering phenomenon has been revisited (6,7,22–24), providing an accurate catalog of static-averaged mechanical properties measured at different physiological conditions. The renewed interest in its metabolic causes and the possible functional consequences for RBC dynamics have motivated theoretical efforts hypothesizing the existence of ATP-dependent cytoskeleton forces (14,25–27). An adequate understanding of this hypothesis requires that a distinction be made between the active contribution of the cytoskeleton and passive thermal fluctuations, a problem that awaits definite experimentation. Likewise, no clear experimental evidence of the primary forces involved in this activity has been reported yet, and their temporal and spatial characteristics remain a matter of debate. Experimental approaches to the flickering phenomenon suffer from restricted time resolution and the limited spatial discrimination of membrane motions in the submicron scale. The use of ultrafast optical microscopy (28) renders the classical flickering method (29,30) capable of tracking cell contour fluctuations at very high sampling rates with subpixel resolution, thus allowing noninvasive detection of signal correlations over broad timescales. Normal RBCs have a characteristic biconcave or discocyte shape, a symmetry property that facilitates the detection, in Fourier space, of the active contributions to the normal modes of membrane motion at the equatorial rim. Here, using ultrafast flickering analysis at the cell equator, we show direct evidence of ATP-dependent forces exerted on the RBC membrane, which are detected as correlated pulses with a well-defined average duration that cause a characteristic nonthermal signal in the membrane fluctuation spectra.

Submitted December 5, 2014, and accepted for publication May 11, 2015.

*Correspondence: monroy@ucm.es

Editor: Cecile Sykes.

0006-3495/15/06/2794/13 $2.00

http://dx.doi.org/10.1016/j.bpj.2015.05.005

MATERIALS AND METHODS

Chemicals

Unless stated otherwise, all materials were purchased at Sigma-Aldrich (Madrid, Spain).

Preparation of red blood cells

Human RBCs were obtained from blood of healthy donors freshly extracted by venipuncture. When necessary, blood samples were stored in EDTA-containing tubes to avoid coagulation before the erythrocyte concentrate was obtained. The latter is obtained after centrifugation (5000 × *g* for 10 min at 4°C). The RBC concentrate was rinsed three times with phosphate-buffered saline (PBS) (RBCs/PBS, 1:5 v/v). A blood aliquot (20 μL) was diluted in PBS (250 μL) containing phosphate buffer (130 mM NaCl, 20 mM Na_3PO_4, 10 mM glucose, and 1 mg/mL bovine serum albumin (hereinafter PBS(+) buffer). This buffer does not contain exogenously added ATP but is able to induce the production of ATP through glycolysis. RBC suspensions were rinsed three times (10 min at 2300 × *g*) in PBS(+). Thereafter, the RBC pellet was resuspended (1:15) in PBS(+). Aliquots (10 μL) of this RBC suspension were transferred to the observation chamber (37°C), which was immediately sealed with a coverglass to avoid evaporation and osmotic stress.

Cytoskeleton inactivation

To study the effect of inactivating the cytoskeleton, we tested RBCs under ATP-depletion and protein-cross-linking conditions. The ATP depletion was performed by incubating cells for 2 h at 37°C in the PBS(−) solution, which is the PBS(+) buffer devoid of glucose and containing 6 mM iodoacetamide and 10 mM inosine, as previously described (7,17). Iodoacetamide is an alkylating drug that blocks the essential active site -SH group in both glyceraldehyde-3-phosphate dehydrogenase and hexokinase (and hence inhibits glycolysis and ATP generation) (31). Inosine is a substrate for human RBC metabolism, and it becomes phosphorylated via purine nucleoside phosphorylase. In the presence of inosine, inorganic phosphate is depleted if it is in short supply, and this starves the phosphorylation of glyceraldehyde-3-phosphate via glyceraldehyde-3-phosphate dehydrogenase, thus inhibiting ADP phosphorylation further down the glycolytic pathway. The result of combining inosine and iodoacetamide is an effective inhibition of cytoskeletal phosphorylation. Drugged cells were maintained in the ATP-depleted medium during experiments. Cells were fixed with glutaraldehyde, which quickly cross-links proteins (32). RBCs were fixed for 30 min at 37°C with a solution of glutaraldehyde (0.2% final) diluted in PBS(−) (18). Glutaraldehyde is known to solidify the hemoglobin in RBCs and cross-link the cytoskeleton (33). Although both treatments somewhat rigidify the RBCs and both inhibit ATP production, stiffening is expected to be weaker for iodoacetamide-treated RBCs than for fixed RBCs treated with cross-linking agent. Passivation experiments by enolase inhibition were performed by adding potassium fluoride (KF, 150 mM) dissolved in PBS(−) buffer. The F^- anion inhibits glycolysis (in concentrations >3 mM), and thus, extensive ATP-metabolic depletion is expected (34).

Flickering spectroscopy

Membrane fluctuations were tracked at the equatorial plane of RBCs using an inverted Nikon 80i microscope (Tokyo, Japan) in the bright-field mode (PlanApo objective 100×, zoom 2×) equipped with an ultrafast complementary metal oxide silicon camera (FastCAM SA3, Photron, Tokyo, Japan; 200 kfps maximal rate, 1 Mpixel; 12 Gbytes RAM). Instantaneous fluctuations are decomposed as a discrete series of Fourier modes, $h(t) = \Sigma_{(q)} h_q(t) \exp(iq_m x)$, where $q_m = m/R$ is the equatorial projection of the fluctuation wavevector (with R the radius and $m = 2,3,4,\ldots\infty$ the azimuthal number) (15). RBC dynamics is experimentally probed through the autocorrelation function, defined as $ACF_q(t) = \langle h_q(t - t')h_q(t')\rangle$, where the angled brackets indicate an average over the time series obtained from a given fluctuation sequence. The first mode ($m = 1$), which corresponds to the motion of the center of mass, is completely separated from the flickering per se modes ($m \geq 2$). Consequently, contributions from translational motion are adequately eliminated from the experimental records. Good statistics was achieved only when time averaging was performed over long time series (typically 5 s at 20 kHz sampling; $n \approx 10^4$ frames). The ultrafast method described here is able to track fluctuations over very long time periods, thus allowing for coherent detection of different components that appear to be correlated over very different timescales. This technical goal cannot be achieved with classical flickering studies involving much slower videomicroscopy (16,22).

RESULTS AND DISCUSSION

Equatorial fluctuations: time series and probability distribution function

In real space, the RBC-equatorial fluctuations, namely $h(x,t) = R(x,t) - R_0$, are measured as local deviations of the equatorial radius, $R(x,t)$, from an average value, R_0, calculated with respect to the center of mass of the discoidal profile (29,30). Fig. 1 shows flickering time traces tracked during 5 s at a high rate (up to 5 kHz) and minimal exposure time (0.2 ms), a set of observational conditions adequate to enable efficient exploration of the accessible membrane configurations. Healthy RBCs, or healthy dyscocytes (dys_h), were studied in PBS(+) buffer, a medium that supports metabolic production of ATP by glycolysis. Healthy RBCs undergo large fluctuations characterized by long-lived excursions far away from the equilibrium position (Fig. 1 *A*). The statistical distribution of membrane fluctuations is found to be broad and nearly symmetric (Fig. 1 *A*). On average (calculated over a statistically significant population of single cells), the membrane fluctuations follow a normal distribution characterized by a large RMSD value, $\Delta h(dys_h) = 32.2$ nm ($\pm 10\%$; $N = 40$), which is consistent with the literature (7,20,22). An adequate account of active cytoskeleton components requires comparison with discoid RBCs in an ATP-depletion medium (dys_d). We incubated RBCs for 2 h in PBS(−) buffer, which led to energy depletion of the cell (31). We found that a 2 h incubation was sufficient for the drugs to inactivate the cytoskeleton; most of the RBCs in the sample became rigid in the echinocyte shape (see Fig. 1 *B*, *left*), and the remaining discocytes (dys_d) exhibited significantly reduced fluctuations (Fig. 1 *B*). Such drugged discoid erythrocytes (dys_d) were used to define the passive skeleton state (7,17). In comparison with healthy RBCs (dys_h), the drugged specimens (dys_d) exhibit weaker fluctuations, as shown by the time trace in Fig. 1 *B* (*center*) The average displacements registered in ATP-depleted cells $\Delta h(dys_d) = 11.2$ nm ($\pm 6\%$; $N = 32$) were found to be significantly smaller than for healthy cells. An additional control was performed with rigid erythrocytes obtained after treatment

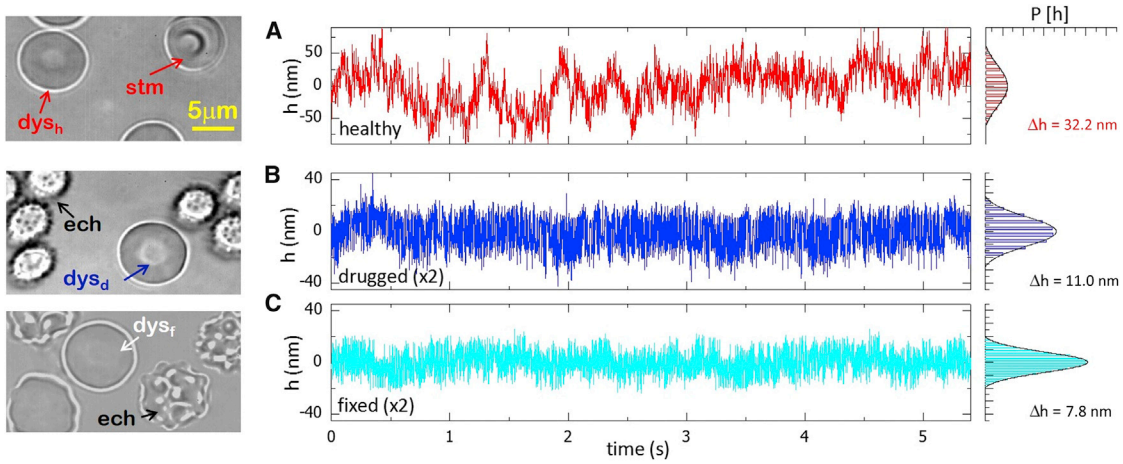

FIGURE 1 Characteristic membrane-fluctuation time traces tracked at an arbitrary (real-space) point in the equatorial profile of RBCs (both global variations in the cell radius (cell swelling) and net displacements of the cell center (cell translation) have been subtracted from the data). The data correspond to RBCs with a discocyte shape (dys) at different activity states, as shown in the micrographs (*left*). (*A*) A healthy flicker (dys$_h$) upon cytoskeleton activity. (*B* and *C*) Passive cases (*h*-scale magnified by a factor of 2 with respect to (*A*)) included drugged RBCs (dys$_d$) after ATP depletion in PBS(−) buffer (*B*) and cells fixed with glutaraldehyde (dys$_f$) (*C*). Although most RBCs in the passive conditions appeared as nonfluctuating speckled echinocytes, some retained their discocyte shape and continued to fluctuate (dys$_d$ and dys$_f$). The normalized histograms at right represent the probability distributions of the membrane displacements averaged over all the points in the equatorial profile (σ_h is the standard deviation). The line envelopes correspond to the normal distribution. To see this figure in color, go online.

with glutaraldehyde, a potent protein cross-linker that induces solidification of both the cytoplasm hemoglobin and the membrane cytoskeleton (32). Under this experimental condition, we had practically motionless specimens, herein informally called fixed erythrocytes (dys$_f$), which still maintained the discocyte shape (Fig. 1 *C*). We observed weaker fluctuations characterized by slender distributions ($\Delta h(\text{dys}_f) = 7.8$ nm ($\pm 5\%$; $N = 25$); see Fig. 1 *C*) typical for rigid specimens with a null metabolism. In treated erythrocytes, only fast local fluctuations are observed (passive cases in Fig. 1, *B* and *C* (dys$_d$ and dys$_f$, respectively), which are different from the slow large-scale undulations detected in healthy specimens (Fig. 1 *A*, dys$_h$). This distinctive feature assigns to the healthy flicker cells a richer long-time dynamics compared to that of passive cells, as identified by other authors (6,7,17,18). The presence of these long-scale and ATP-dependent motions enables us to explore the cytoskeleton activity in two ways, 1) by determining its impact on the global mechanical properties of the RBC membrane, and 2) by testing for signatures of active forces on the dynamical correlations of the membrane motions.

RBC mechanical properties: membrane rigidities and effective temperature

To get further insight into the spatial and dynamic characteristics of active forces involved in the RBC flicker requires a precise account of the mechanical properties of both the passive lipid membrane and the underlying cytoskeleton. In the classical treatment of the fluctuation spectrum by Brochard and Lennon, only the fluid lipid bilayer is considered, which is assumed to have an elasticity determined by bending (κ) and tension (σ) rigidities (16). Using the Milner-Safran (MS) framework to describe membrane fluctuations in the quasispherical geometry, the bending/tension modes are viewed as linear combinations of the spherical harmonics, $Y_{lm}(\phi, \theta)$ (35). However, in the flickering experiment, we can only obtain information from the focal plane, which is adjusted at the equatorial site where the sharpest image can be focused. Several authors have clarified how the MS analysis can be adapted to the case where the equatorial contour of an axisymmetric membrane is tracked by time-resolved microscopy (29,30). In this case, the equatorial undulations correspond to the discrete sequence of circular eigenmodes with the wavevector determined by the azimuthal number, $q = m/R$ ($m = 2,3,4\ldots\infty$ and R_0 is the spherical radius). Every equatorial MS mode is expressed as a sum of the azimuthal projection of the spherical harmonics $Y_{lm}(\phi, \theta = \pi/2)$ over the possible states of polar orientations compatible with the equatorial undulation, i.e., where $l \geq m$ (combining Eq. S1.9 with Eq. S1.4 in the Supporting Material for $t = 0$; also see Eq. S.12), this sum is

$$P_m(q = m/R) = \frac{\langle h_m^2 \rangle}{R^2} = \frac{k_B T}{\kappa} \sum_{l=m}^{l_{max}} \left\{ (l+1)(l-1)\left[l(l+1) + \Sigma_{eff} \right] \right\}^{-1}, \quad (1)$$

where $\Sigma_{eff} = \sigma R^2/\kappa + 4c_0 R - 2(c_0 R)^2$ accounts for the apparent membrane tension (σ), which is corrected by the local spontaneous curvature ($c_0 R = -2.4$ for RBCs at

the equator (36); see Section SI1 in the Supporting Material for details).

In RBCs, a spectrin-based cytoskeleton is linked underneath to the lipid bilayer, and thus, two additional components must be taken into account in the elastic free energy: 1), the intrinsic shear rigidity of the spectrin network (37), and 2) the confinement coupling between the membrane and the cytoskeleton (13). In this case, the MS description remains valid for a q-dependent renormalized value of the bending modulus (in Eq. 1), which includes both additional contributions (14,25):

$$\kappa \Rightarrow \kappa_{\mathrm{eff}}(q) = \kappa + \frac{9k_{\mathrm{B}}T}{16\pi\kappa}\mu q^{-2} + \gamma q^{-4}, \qquad (2)$$

where μ is the shear modulus and γ is a spring constant accounting for the confinement energy involved in constraining large membrane excursions from the cytoskeleton. At high q, both cytoskeleton contributions vanish and the effective bending modulus, κ_{eff}, renormalizes to the bare value, κ.

Fig. 2 *A* shows the fluctuation spectra experimentally obtained for RBCs under the different conditions considered in this work. On the one hand, for passive cells ($\mathrm{dys_d}$ in PBS(−) buffer and $\mathrm{dys_f}$ in PBS(−) with glutaraldehyde), the fits of the experimental data to the MS spectrum characterize the passive component of the RBC membrane as a rigid material (see Table 1), in contrast to the high flexibility of typical fluid bilayers ($\kappa \approx 10k_{\mathrm{B}}T$, $\mu \equiv 0$). On the other hand, the fluctuation spectrum of normal RBCs (in the presence of ATP) shows amplitudes higher than those found for the former passive cells (more than one order of magnitude higher at low q; see Fig. 2 *A*). Any extra rigidity component, i.e., other than those considered for the passive fluctuations, should contribute to the reduction of the global fluctuations. Consequently, this dynamic enhancement can be interpreted either as 1) effective softening, leading to lower effective elastic constants; or 2) higher effective temperature, accounting for internal active forces, e.g., the cytoskeletal kicking force hypothesized previously (7,14,38).

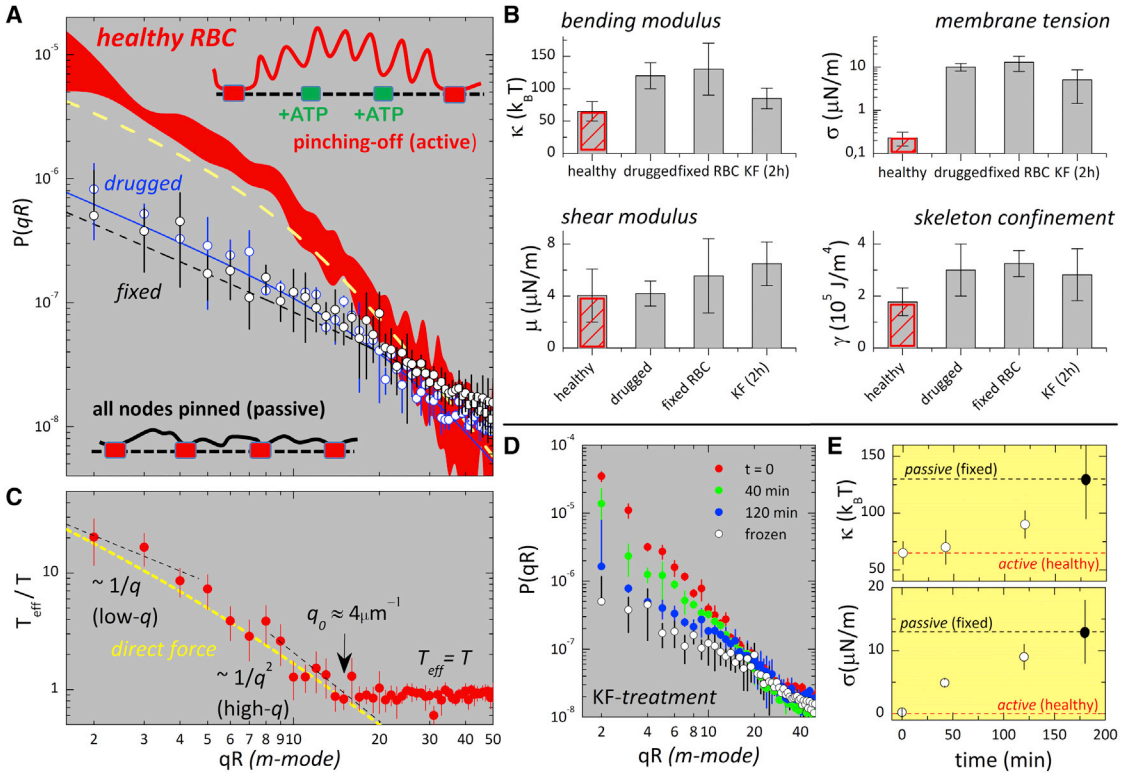

FIGURE 2 (*A*) Experimental static spectra calculated from the time-averaged amplitudes of the equatorial modes, $P(qR) = \langle h_q^2 \rangle$, of discocytes at different states (see Materials and Methods). In the active case (*red*), the variance band represents data obtained over different healthy cells ($N = 40$). In passive cases, blue- and black-outlined circles represent the average spectra measured for drugged and fixed discocytes, respectively. Lines represent the fits to the MS spectrum using Eqs. 1 and 2, with bending modulus κ_{eff} as defined in Eq. 2. For the healthy RBCs (*dashed yellow line*), in the low-q region dominated by membrane tension, the MS spectrum predicts smaller fluctuations than can be registered experimentally. (*B*) Statistics for the mechanical parameters as obtained from the fits to the $P(qR)$ spectra (see Table 1 for numerical data). (*C*) Effective temperature, defined as $T_{\mathrm{eff}}/T = P_{\mathrm{h}}/P_{\mathrm{d}}$ (from the data in *A*) and plotted as a function of the fluctuation wavenumber, $m = qR$. The dashed yellow line represents the trend expected for a direct force (the black dashed line indicates limiting behavior, $T_{\mathrm{eff}} \sim 1/q$ at low q and $T_{\mathrm{eff}} \sim 1/q^2$ at high q (at $\gamma \neq 0$); see Gov (38)). (*D*) Inactivation kinetics for RBCs treated with KF. The different curves correspond to the $P(qR)$ spectra recorded at increasing KF incubation times. (*E*) Time dependence of the mechanical parameters along the inactivation process in (*D*) (*open circles*); the solid circles correspond to a passive limit represented by the mechanical parameters of the fixed discocytes with a cross-linked cytoskeleton after treatment with glutaraldehyde. To see this figure in color, go online.

TABLE 1 Mechanical characteristics of the RBC discocytes

Discocyte	N	κ (10^{-19}J)	σ (μN/m)	μ (μN/m)	γ (10^5 J/m^4)
Healthy	40	2.7 ± 0.6	0.23 ± 0.1	4.0 ± 1.0	1.7 ± 0.5
Drugged	32	5.0 ± 0.8	10.0 ± 0.6	4.2 ± 1.0	1.0 ± 0.2
Fixed	25	5.4 ± 1.5	13 ± 4	5.6 ± 1.5	1.5 ± 0.5
KF-treated	6	3.5 ± 0.7	5 ± 2	6.5 ± 1.5	1.0 ± 0.2

Errors indicate N-populational standard deviations.

For healthy cells, the values of the elastic parameters obtained from the analysis of the high-q regime (where thermal noise dominates) in terms of thermal fluctuations and an effective elasticity (with Eqs. 1 and 2; see data in Table 1 and Fig. 2 *B*), are found to be in agreement with literature data obtained by a similar analysis (6,7,22). Remarkably, the effective membrane tension is found to be significantly smaller in healthy RBCs ($\sigma_h = 0.23 \pm 0.1$ μN/m) than in passive cells, in particular when data are compared to those for fixed cells obtained after cytoskeleton cross-linking with glutaraldehyde ($\sigma_f = 13 \pm 4$ μN/m). In view of the large excess area available in the discocyte shape, the low-tension state of normal RBCs could be perceived as a loose interaction between the flexible membrane and the rigid cytoskeleton, in contrast with the permanent anchoring in the passive cases (see cartoon in Fig. 2 *A*). In addition, the bending stiffness is found to be significantly lower in normal RBCs than in the passive cases ($\kappa_{act} \approx \kappa_{pass}/2$, see Table 1 and Fig. 2 *B*). Such mechanical softening, observed under cytoskeleton phosphorylation, can be understood as a dynamical effect related to the reversibility of cytoskeleton anchoring; the mechanical effects are much more flexible and floppy healthy RBCs, compared to stiffer passive cells. However, no significant changes are detected in the shear modulus (μ) or in the confinement constant (γ), the two mechanical parameters reporting global cytoskeleton connectivity (see Table 1 and Fig. 2 *B*). Consequently, we cannot eliminate the possibility of dynamic coupling with targeted energy transfer at different scales as an explanation of the effective membrane-softening characteristic of healthy cells with a reversibly connected cytoskeleton. A crude analysis of the spatial distribution of the effective softening can be made in terms of effective temperatures calculated from the comparison between the experimental spectra of the normal and passive cells, after taking into account the overall changes in the elastic moduli, i.e., $T_{eff}/T \equiv P_h/P_d$ (Fig. 2 *C*). (Drugged, instead of fixed, cells were taken as the reference passive state. The reason for this choice is that the possible additional bulk rigidity appeared in fixed cells as a consequence of hemoglobin cross-linking in the cytoplasm.) A high effective temperature is observed at low q ($T_{eff}/T \approx 20$ at $qR \approx 2$), indicating the global activity of the RBC. Before thermal effects become dominant ($T_{eff} \approx T$), the active effects decrease first as $T_{eff} \sim q^{-1}$ at low wavenumbers ($m < 4$) and then renormalize to $T_{eff} \sim q^{-2}$ for intermediate values ($4 < m < 15$). This behavior is a clear signature of an active direct force (38), in contrast to active curvature-inducing forces, for which one expects an increase in T_{eff} with increasing q (38). Finally, active effects become negligible compared to the thermal contribution at wavevectors above a mesoscopic cutoff, $q_0 \approx 4$ μm^{-1} ($m > m_0 \approx 15$), where $T_{eff}/T \approx 1$. This cutoff corresponds to the smallest membrane patch for which global activity is detected (where active motion is dominant over thermal fluctuations), $\lambda_0 = 2\pi/q_0 \approx 1500$ nm, a distance well above the characteristic mesh size of the cytoskeleton network. Because the cytoskeleton unit element is actually smaller (39), $a \leq 100$ nm $<< \lambda_0$, if λ_0 indicates the length scale of the active patch, then the probability of a given cytoskeleton node being active at a given moment might be small, as suggested for the detailed model of the active membrane (26,27). Indeed, if many cytoskeletal nodes became detached simultaneously, a catastrophic decrease of the shear modulus would be detected at rest conditions, similar to the fluidization transition experimentally observed in healthy cells stressed at high rates (40). Since no such sharp decrease of the in-plane rigidity is observed (the shear modulus being essentially constant in the different realizations), we conclude that most of the cross-linking nodes of the spectrin skeleton are pinned to the plasma membrane, and that detachment events, which occur upon phosphorylation, are rather rare and sparsely distributed in space and time (14). This argument also applies for the averaged membrane confinement, which is essentially preserved with a dynamically interacting cytoskeleton. The detection of enhanced (active) amplitudes supports the hypothesis of the existence of metabolically regulated motions that are measurable over large spatial scales ($q << q_0 = 2\pi/\lambda_0$). Further evidence of the metabolic softening of healthy RBCs is provided by additional experiments in which potassium fluoride was added to the PBS(−) buffer (KF 150 mM final). In that case, enolase was blocked by fluoride anion during glycolysis, which inhibited the main metabolic source of ATP (41). A progressive decrease of the flickering activity is observed in the experiments presented here (see Fig. 2 *D*), especially at low q, where the spectral amplitudes are dominated by the active component and restrained by membrane tension. A quantitative analysis of the effective mechanical constants indicates a progressive stiffening upon ATP inhibition. This is detected as an increase of the bending modulus (Fig. 2 *E*, *upper*) and the membrane tension (Fig. 2 *E*, *lower*) from their low effective levels, corresponding to healthy RBCs, to maximal values, corresponding to the bare mechanical response of the passive cells. Note that membrane stiffening is observed after both the increase of permanent connection with the spectrin network and the reduction of active forces due to ATP inhibition.

Time-autocorrelation function: thermal modes plus ATP-dependent force

In the simplest description, the dynamics of the active membrane fluctuations is given in the Langevin form (14,27),

$$\frac{\partial h_q}{\partial t} + \omega_q h_q = \Lambda_q[f_{\rm th}(t) + f_{\rm act}(t)], \qquad (3)$$

where ω_q is the damping coefficient of the membrane response that arises from the balance of the thermal ($f_{\rm th}$) and active ($f_{\rm act}$) excitation forces with the elastic restoring forces and viscous friction, which ultimately determine the relaxation timescale. The latter is described by the Oseen interaction kernel; for a free membrane, $\Lambda_q \approx (4\eta q)^{-1}$, where η is the effective viscosity of the RBC cytoplasm (see Section SI2 in the Supporting Material for details). The thermal force is an uncorrelated Gaussian noise, $\langle f_{\rm th}(t) f_{\rm th}(t')\rangle_q = 2k_{\rm B}T\Lambda_q^{-1}\delta(t-t')$, producing Brownian motion with exponentially decaying time correlations when convoluted with viscous friction. The active force introduces additional correlations in the form of a characteristic timescale describing the pulse duration. If one considers stochastic pulse lengths, τ, with a Poissonian distribution $P(\tau)$, the correlations of the direct forces take a shot-noise form, that is, $\langle f_{\rm act}(t) f_{\rm act}(0)\rangle_q = (n_m/2) F^2 \exp(-t/\tau)$. To describe such an active component (27,34), the model implements a direct force of amplitude, $\pm f_0$, and duration, τ, produced by kicking motors randomly distributed on the membrane with an areal density, n_m. This results in an effective force, F ($\sim p_{\rm on} f_0$, where $p_{\rm on}$ is the probability of an individual motor being on), globally exerted by the active motors on the membrane, which consequently moves at a velocity proportional to F/η (η is the bulk viscosity). To discriminate active forces from regular thermal motions in the RBC flicker considered here, we analyze time autocorrelation in the equatorial fluctuation modes, which actually arise from a combination of spherical harmonics projected on the azimuthal plane (see Sections SI1 and SI2 in the Supporting Material for a detailed discussion). Fig. 3 shows the experimental height-to-height temporal autocorrelation functions, $ACF_q(t) = \langle h_q(t) h_q(0)\rangle$, measured for the equatorial eigenmodes of discocytes ($q = m/R$). A pure-thermal relaxation is expected in the passive case of a viscous membrane (Fig. 3 *A*, *left*), where the relaxation profile is described by an exponential decay modified by the special function exponential integral, $\mathrm{E}_a(x)$ (see Eq. S2.15c in the Supporting Material),

$$ACF_q^{(\rm th)}(q,t;\alpha) \approx e^{-\omega_q t} - (\omega_q t)\mathrm{E}_{3/(2+\alpha)}(\omega_q t), \qquad (4)$$

with a shape parameterized by α, a renormalization parameter that varies in the interval comprised between $\alpha = 1$ (regular fluid membrane) and $\alpha = 0$ (viscous membrane) (see Section SI2 in the Supporting Material for details). The decay rate, ω_q, is essentially determined by the relaxation rate of the fundamental spherical harmonic, $l = m$ (see Eq. S1.10a),

$$\omega_q(l = m = qR) = \frac{\kappa_{\rm eff}}{\eta_{\rm eff} R^3}\frac{l(l+1) + \Sigma_{\rm eff}}{Z(l)}, \qquad (5)$$

where $Z(l) = (2l+1)(2l^2+2l-1)/l(l+1)(l+2)(l-1)$. In the high-$q$ limit, $Z(l) \approx 4/l$, so Eq. 5. converts to the usual dispersion equation for the planar membrane model in a bulk fluid of effective viscosity $\eta_{\rm eff}$, i.e., $\omega_q \approx (\kappa q^4 + \sigma q^2 + \gamma)/4\eta_{\rm eff} q$. If the membrane has an intrinsic surface viscosity μ_m, the bulk viscosity takes a q-dependent effective value, $\eta_{\rm eff} = \eta(1 + \mu_m q/2\eta)$ (42). This can be rewritten in terms of a characteristic length, $L_C = \mu_m/2\eta$, that determines the crossover between bulk- and membrane-dominated frictional regimes, that is, $\eta_{\rm eff} = \eta(1 + qL_C)$ (for details, see Eqs. S2.13 and S2.14 in the Supporting Material).

We first probed for relaxation rates of the low-q modes in drugged cells (Fig. 3 *A*, *left*), where a single relaxation corresponding to the thermal fluctuations is indeed observed. In this case, data can be accurately described by the modified exponential profile in Eq. 4. As expected, the fitted values of the relaxation rates, ω_q (Fig. 3 *B*, *left*), follow the theoretical prediction in Eq. 5 for thermal modes in a quasispherical membrane subjected to cytoskeleton confinement. Taking the experimental values of Table 1, $c_0 R = -2.4$ (36) and $\eta = 6$ cP (43), one gets $L_{\rm C} = 260 \pm 80$ nm (best fit value). Below this characteristic length ($q > L_{\rm C}^{-1}$), which is compatible with the mesh size of the cytoskeleton, frictional dissipation is controlled by the intrinsic viscosity of the membrane; from the current experiments, $\mu_m = 2\eta L_C \approx 3 \times 10^{-9}$ kg/s, in agreement with previous estimations (42).

Once the passive realization was found to be consistent with the regular dynamics of the thermal motions in a viscous membrane, the dynamics of the RBC flicker was tested in the PBS(+) medium containing glucose, thus enabling glycolysis and therefore the production of ATP (Fig. 3 *A*, *right*). The presence of ATP in the active case makes relaxation significantly slower than in the former passive case (compare the two curves in Fig. 3 *C*), which suggests a dynamical softening caused by the cell activity. Furthermore, a correlation bump is systematically observed in the long-time tail of the relaxation functions obtained for healthy cells (Fig. 3 *A*, *right*), a feature absent in drugged cells (Fig. 3 *A*, *left*). The observation of this extra contribution to the mechanical relaxation of the healthy RBC flicker–in addition to the primary thermal component—is the main experimental result of this study and demonstrates the presence of temporally correlated forces in the stress field driving the membrane fluctuations. A similar correlated component was recently identified to be a direct consequence of nonequilibrium molecular activity in a model system with artificially reconstituted membrane motors (44). The

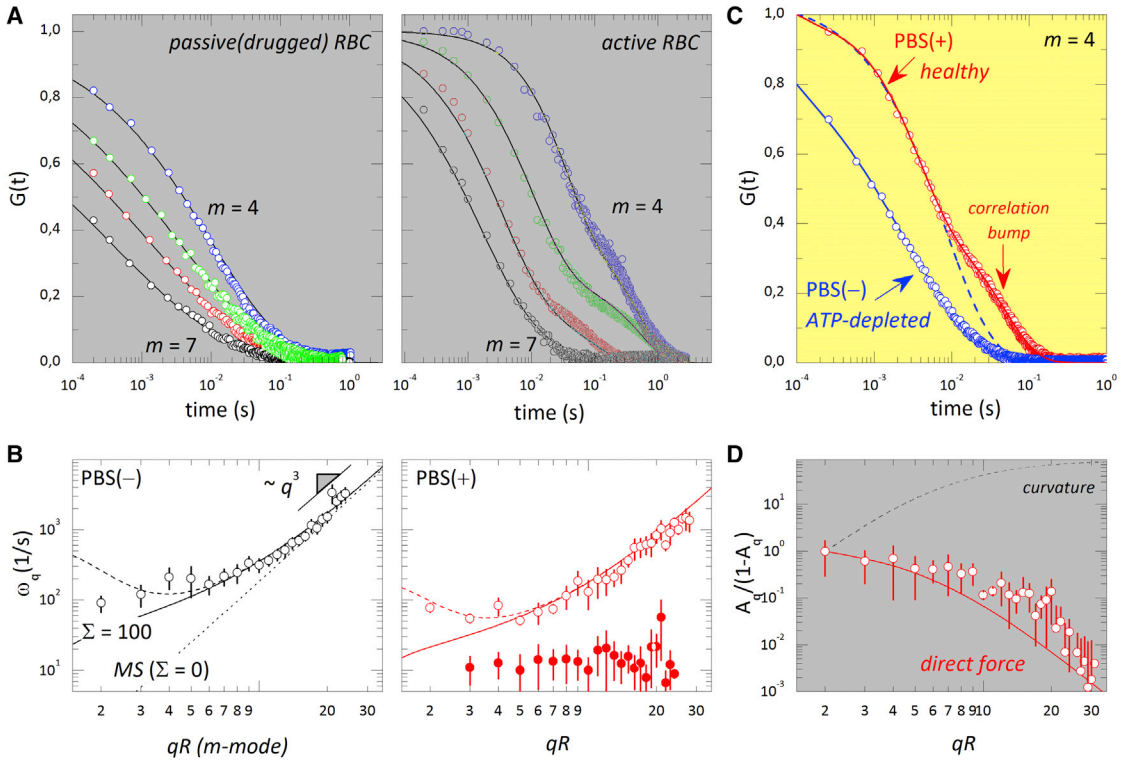

FIGURE 3 (*A*) Experimental autocorrelation functions of the RBC flicker in the passive (drugged, *left*) and active (healthy, *right*) cases; wave numbers $m = qR = 4$ (*blue*), 5 (*green*), 6 (*red*), and 7 (*black*). Solid lines correspond to fits of the experimental data to the stretched exponential model in Eq. 4 for the thermal modes in passive cells (*left*) and to the bimodal function in Eq. 6 for the healthy cells (*right*). (*B*) Relaxation rates in the passive (*left*) and active (*right*) cases, with open circles corresponding to thermal modes, ω_q, and solid circles to the active component, ω_{act}. MS frequencies were fitted using Eq. 5 with $\eta = 6$ cP and κ_{eff} from Eq. 2, taking values from Table 1 (*dotted line*, tensionless membrane, $\Sigma = 0$; *solid line*, tensioned membrane, $\Sigma > 0$; *dashed line*: tensioned and viscous membrane, $\Sigma > 0$, $\gamma > 0$, with $L_C = 260 \pm 80$ nm). (*C*) Comparison between autocorrelation ($m = 4$) in passive cells with Eq. 4 (*blue*) and in healthy cells with Eq. 6 (*red*). (*D*) Relative amplitudes of the active component decaying according to the direct-force model (*red line*, Eq. 7) and the curvature-force model (*black dashed line*). To see this figure in color, go online.

active component observed in RBCs is ATP-dependent and emerges at a timescale that is clearly distinguished from the relaxation of the thermal mode, which indicates additionally correlated membrane motion caused by direct forces with a similar duration. Consequently, if this active force is assumed to be uncorrelated with the thermal forces in Eq. S3.3, the autocorrelation function $ACF(t)$ takes the bimodal form

$$ACF_q^{(act)}(t) = \left(1 - A_q\right)ACF_q^{(th)}(t) + A_q \exp(-\omega_{act}t), \quad (6)$$

where the first term is the regular thermal component and the second term accounts for the additional correlations that appear at timescale τ ($= 1/\omega_{act}$) as a result of metabolic activity (Fig. 3 *B*, *right*). From the fits, both the relaxation rates and the relative amplitudes of the two modes are obtained, the faster due to the properties of the thermal fluctuations and the slower to metabolic activity. When timescales are compared, the presence of ATP (Fig. 3 *B*, *right*) makes the whole relaxation significantly slower than in the former passive case (Fig. 3 *B*, *left*). This slowing-down effect suggests a dynamic softening in healthy cells, compatible with the effective decrease of elasticity moduli deduced from the static data in Fig. 2, i.e., ω_q(normal)/ω_q(ATP-depleted) $= \kappa_h/\kappa_d \approx 1/2$. Indeed, from the comparison of the relaxation rates of the thermal modes, assuming an effective bending-like regime in the high-q limit (Fig. 3 *B*), we estimate ω_q(healthy)/ω_q(drugged) $\approx \kappa_h/\kappa_d \approx 0.5$, showing that the relaxation rate of the mechanical response is affected by the cytoskeletal activity, an intrinsic property of the equation of motion (Eq. 3) and in agreement with the values presented in Table 1.

Thereafter, we analyzed the correlation bump that occurs in healthy cells. We observed that in drugged cells, it disappeared as a consequence of ATP synthesis inhibition. Surprisingly, such a slower, and ATP-dependent, component is found with a near-constant relaxation rate, $\omega_{act} \approx 10$ s^{-1}, regardless of the probed wavevector (Fig. 3 *B*, *right*). With respect to its amplitudes, at low wavevector, the active component is found to be comparable to the thermal bending mode ($A_q \approx 0.5$ at $qR \leq 4$); however, its relative amplitude decreases with increasing q, indicating a larger dominance of the thermal mode at higher q (Fig. 3 *D*). The two characteristics that support an active nature (see

Section SI3 in the Supporting Material) are 1) a single-exponential decay, $ACF^{(act)} \sim \exp(-t/\tau)$, compatible with shot-noise correlations; and 2) a nondispersive q-dependence, $\tau \approx \omega_{act}{}^{-1} \sim q^0$, indicative of a direct force (26,27) with a given characteristic timescale independent of the spatial scale probed. These features could represent the dynamical signature of the reaction cycle of a metabolic process producing nonequilibrium membrane forces of average duration τ. The observed correlation bump may be related to a force applied by kicking active elements on the membrane, similar to the correlation effect of pumping activity described in Bouvrais et al. (44). This active force should be pulsed, as it is applied during a short time,$\tau \approx \omega_{act}{}^{-1} \approx 100$ ms, which may be related to the quick metabolic remodeling of the cytoskeleton (14,26). The model in Ben-Isaac et al. (27) and Gov (38) can be used to predict the relative amplitude of the active mode; for a direct force of amplitude F (see Eqs. S3.2 and S3.3 in the Supporting Material), one gets

$$\frac{A_q}{1-A_q} \propto \frac{n_m\left(F\Lambda_q\right)^2}{2k_BT\Lambda_q}\frac{\omega_q}{\left|\omega_q^2-\omega_{act}^2\right|}. \quad (7)$$

Taking the values $n_m(F/4\eta)^2 = 2.5\ 10^5\ \mathrm{nm}^2/\mathrm{s}^2$ and $\omega_{act} = \tau^{-1} = 10\ \mathrm{s}^{-1}$, this expression predicts the active mode driven by a direct force with a relative amplitude that compares well with the observation (Fig. 3 *D*). In the tension-dominated regime, this ratio is expected to decay as $\sim 1/q^4$ when $\omega_q >> \omega_{act}$ and as $\sim 1/q^0$ for $\omega_q \approx \omega_{act}$, in agreement with experimental results. We also note that the active-component amplitude in Eq. 7 is predicted to diverge (in the linear model) when $\omega_{act} = \omega_q$, but in the healthy RBC, we are everywhere far from this resonance, $\omega_{act} < \omega_q$ (Fig. 3 *B*, *right*). An alternative case corresponds to active forces that induce membrane curvature. In this case, the force is coupled to the local membrane curvature, $\nabla^2 h$ (instead of h), so we get $F \rightarrow F(qr)^2$ in Eq. 7 (with r being the spontaneous radius of curvature associated with the active conformational change) (38). Consequently, the effect of curvature-inducing forces increases with increasing q, which is the opposite of what was observed, thus ruling out this force mode (Fig. 3 *D*). As a proof of consistency, we analyzed the mutual correspondence between the characteristic time of the cytoskeletal motions and the spatial scale where membrane activity dominates ($T_{eff} > T$ at $q < q_0$; see Fig. 2 *C*). From the theoretical model of an active membrane pumped by direct forces (38), in the tension-dominated regime, one expects a renormalization between two limiting regimes at a crossover wavevector, $q_c \approx 2\eta\tau^{-1}/\gamma$, which determines the boundary between an active force-dominated regime ($q < q_c$) and a kinematic regime governed by membrane tension ($q > q_c$). Assuming $\tau \approx 0.1$ s, one estimates that $q_c \approx 1\ \mu\mathrm{m}^{-1}$, so that $m_c = q_c \times R \approx 4$–5, in agreement with experimental crossover behavior (see Fig. 2 *C*).

Power spectra: Brownian flicker versus cytoskeleton forces

To better characterize the chromatic characteristics of the flickering noise, the power spectral densities (PSDs) were computed by Fourier transform of the fluctuations: $\mathrm{PSD}(\omega) = \|\int h(t)e^{i\omega t}dt\|^2$. Fig. 4 shows the results from experiments under different conditions. Membrane motion is found to have much larger spectral densities in healthy RBCs than in ATP-depleted cells (Fig. 4 *A*). The spectral density of healthy cells is found to be enhanced at low frequencies compared to that in the passive cases, indicating that active cells have more energy in the slower motions, even more than expected for the mechanically soft Brownian flicker (with mechanical constants given in Table 1

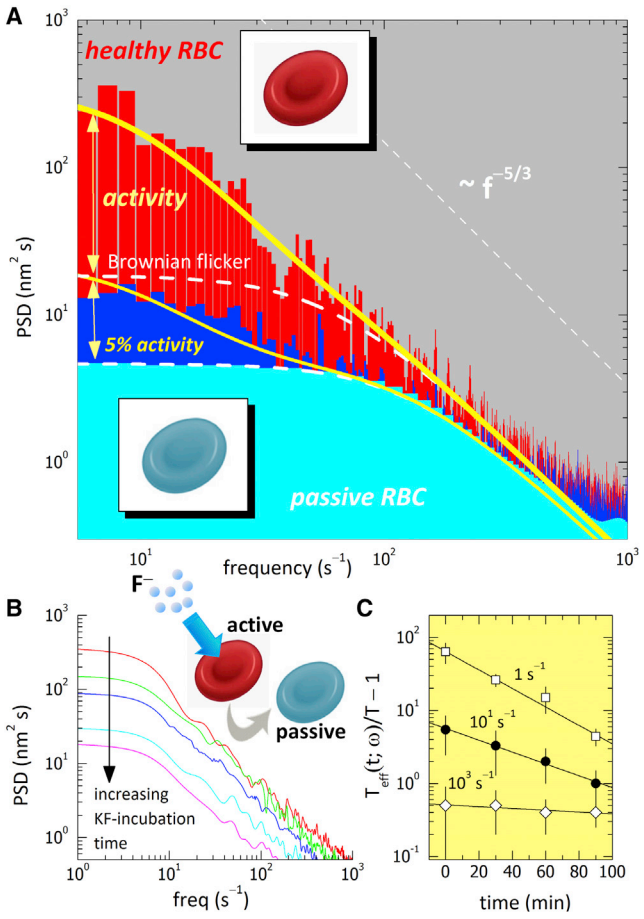

FIGURE 4 (*A*) PSDs of the RBC flickers using the fast-Fourier transform (FFT) algorithm, $\mathrm{PSD}(\omega) = \{\mathrm{FFT}[h(t)]\}^2$, for healthy cells ($\mathrm{dys_h}$) (*red region*), drugged cells ($\mathrm{dys_d}$) (*blue region*), and fixed cells (*cyan region*). Vertical bars correspond to experimental data; lines indicate theoretical predictions (see Eqs. S3.3 and S3.4 for the pure thermal spectrum (*dashed lines*) and the thermal spectrum plus the active component arising from direct cytoskeletal forces (with 5% residual activity in the passive case) (*solid lines*)). (*B*) Time evolution of the experimental PSDs of RBC flickers under KF treatment. (*C*) KF-passivation kinetics measured as the decrease in effective temperature calculated from the data in (*B*) interpolated at different frequencies. To see this figure in color, go online.

for healthy RBCs). We attribute the extra fluctuations to active forces (Fig. 4). Our model of active RBC flicker considers membrane-driving forces superposed on passive thermal motions (27,38); in the ideal tensionless case (see Eq. S3.4 in the Supporting Material),

$$\mathrm{PSD}(\omega) \approx \mathrm{PSD}_{\mathrm{th}}(\omega) + \left(\frac{F}{4\eta}\right)^2 \frac{n_m \tau}{\omega^2(1+\omega^2\tau^2)}. \qquad (8)$$

No correlation between active motions and thermal fluctuations is assumed in this (simplest) approximation (25,27), and thus, we consider additive contributions to the spectral amplitudes. The first component represents passive Brownian flickering composed of the dynamic superposition of the thermal modes in a flexible membrane (16). At high frequencies, a Brownian-noise decay is expected, $\mathrm{PSD}_{\mathrm{th}}(\omega \rightarrow \infty) \sim \omega^{-5/3}$ (7,16). In the low-frequency regime, thermal fluctuations are dominated by the tension of the membrane (σ_{eff}) and the confinement term (γ), so an upper bound with a value determined by σ_{eff} is expected in the passive spectra, $\mathrm{PSD}_{\mathrm{th}}(\omega \rightarrow 0) \sim k_B T/\sigma_{\mathrm{eff}}$. This is the pure thermal behavior found for the glutaraldehyde-fixed discocytes (Fig. 4 *A*). In addition, the second summand in Eq. 8 accounts for the spectral density corresponding to the ideal shot noise produced by active elements exerting pulsed forces on a tensionless membrane ($\sigma \rightarrow 0$) (27,38). If present, the active term should contribute mainly at low frequencies, measurable as an increase of the spectral density. However, at high frequencies, where Brownian noise dominates, the active component is expected to strongly decrease as $\sim\omega^{-4}$. Indeed, the flickering spectrum of healthy cells is observed with the $\omega^{-5/3}$ decay corresponding to thermal components at high frequencies, in agreement with previous experiments (7,25). However, at frequencies <10 Hz ($\approx\omega_{\mathrm{act}}$), the healthy flicker dissipates additional power compared to the pure thermal component corresponding to the Brownian flicker (Fig. 4 *A*). Taking the values we fitted for Fig. 3, i.e., $\tau = 1/\omega_{\mathrm{act}} = 100$ ms and $n_m(F/4\eta)^2 = 2.5 \times 10^5\ \mathrm{nm}^2/\mathrm{s}^2$, the model provides an accurate prediction of the active fluctuations in both frequency regimes (Fig. 4 *A*). This implies a breakdown of the equilibrium description at frequencies $<10\ \mathrm{s}^{-1}$, leading to a frequency-dependent dissipative component due to active motions. Such frequency dependence resembles the results of the Betz experiment with an optical trap, from which the same timescale was inferred for the active component (7). By contrast, RBCs with a passive cytoskeleton (treated with either ATP-inhibitory drugs or glutaraldehyde) are observed to dissipate significantly less power, with a comparatively lighter spectral distribution compared to that of healthy cells at low frequencies. In particular, for fixed cells, the observed PSD is compatible with pure thermal fluctuations of a rigid membrane, as deduced from the PSD ratio calculated at low frequencies, $[\mathrm{PSD_h}/\mathrm{PSD_f}]_{\omega\rightarrow 0} \approx (\sigma_{\mathrm{f}}/\sigma_{\mathrm{h}})_{\mathrm{eff}} \approx 10^2$, which is in accordance with data shown in Table 1. Some remaining activity is detected in drugged cells, and it is measured as additional power dissipated at low frequencies with respect to fixed cells (~5% of the activity of healthy cells in $\mathrm{dys_d}$ at $\omega \leq \omega_{\mathrm{act}} \approx 10\ \mathrm{s}^{-1}$; Fig. 4 *A*). The expression for the active contribution of the PSD, given in Eq. 8, is an approximation for the limit of zero tension, and therefore, it strictly applies to the high-ω regime where tension is not dominant. Numerically integrating the PSD for the active component for low ω, where the tension is dominant (27,38), gives the well-behaved function plotted in Fig. 4 *A*. Further evidence for the existence of active elements dissipating additional power is provided from experiments of glycolysis breakdown with fluoride anions (F^-). Fig. 4 *B* shows the time evolution of the PSDs during treatment of RBCs with potassium fluoride (KF). A significant decrease of the dissipated power is observed alongside the kinetic process of enolase inhibition, especially at low frequencies. Because ATP levels progressively decrease after glycolysis inhibition, a proportional decrease of the metabolic activity is expected in accordance with the observed decrease of the mechanical power. The relative decrease of the dissipated power is plotted in Fig. 4 *C* as a function of time, i.e., $T_{\mathrm{eff}}(t)/T = \mathrm{PSD}(t)/\mathrm{PSD}(t\rightarrow\infty)$, taking the PSD registered after 2 h as the reference passive state ($\mathrm{PSD}(t\rightarrow\infty) \approx \mathrm{PSD_{th}}$, for which $T_{\mathrm{eff}} \approx T$). The results presented in Fig. 4 *C* indicate a first-order kinetics for the inactivation process, $T_{\mathrm{eff}}(t;\omega) \sim e^{-k(\omega)t}$, characterized by a frequency-dependent inhibition rate, *k,* which determines how fast the mechanical activity is inhibited in the presence of KF. Indeed, the lower the frequency probed, the faster the observed rate of decrease of activity, a fact consistent with the presence of correlated effects due to cytoskeleton forces only at timescales longer than the pulse time (Fig. 4 *C*; $k > 0$ at $\omega < 10^2\ \mathrm{s}^{-1} \approx 1/\tau$).

Cytoskeleton pinning and active dynamics

We gain further insight about the spatial characteristics of the detected shot forces by discussing our results in structural terms. The RBC membrane is composed of a flexible lipid bilayer, mainly composed of phospholipids and cholesterol, which is linked to a metabolically active cytoskeletal network. The native structure of unstressed membrane RBC skeleton has been determined by transmission electron microscopy (TEM) (45,46). TEM images of intact membranes reveal a foam-like meshwork of spectrin filaments with a gradual decrease in density from the center of the cell to the equatorial edge. The ultrastructure of stretched patches of the RBC cytoskeleton reveals a network organization (see Fig. 5 *A*) in which spectrin filaments are the main structural component (2,3). In vivo, the characteristic length of the network is $a = 46 \pm 15$ nm (46), indicating that on average, the size of spectrin filaments in the native membrane skeleton is a fraction of its contour length ($L \approx 190$ nm) observed in membrane patches stretched on TEM grids (39). Spectrin filaments are pinned to the membrane

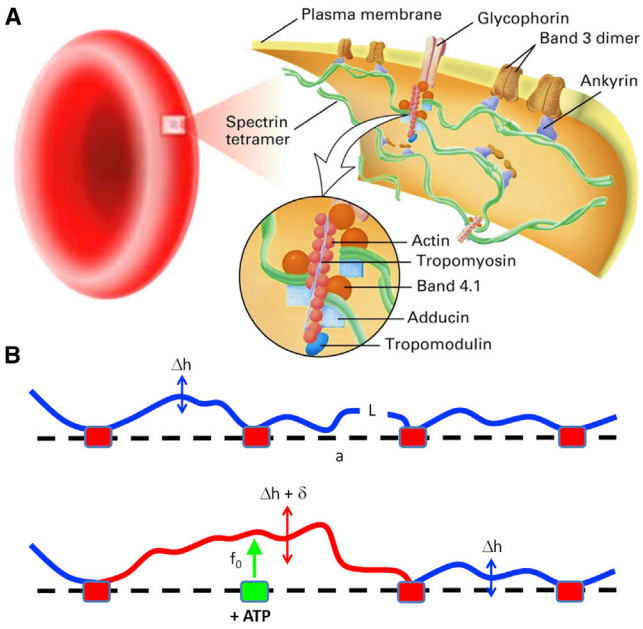

FIGURE 5 (*A*) Cartoon of the molecular structure of the RBC cytoskeleton in which we explain our dynamical model. A near-hexagonal spectrin network is assembled by means of multiprotein junctional complexes (see details in the text), which act as primary attachments to the plasma membrane via a specific membrane domain of band 4.1 protein that reversibly interacts with glycophorin C in an ATP-dependent manner. Secondary attachment is provided by ankyrin, which interacts with transmembrane band 3 dimers. (*B*) Pinning model of cytoskeleton activity at junctional nodes. Complete membrane attachment to a rigid cytoskeleton causes effective stiffening, shown as low-amplitude fluctuations, Δh (*upper*). Node phosphorylation causes the membrane to pinch off from the cytoskeleton, resulting in an effective kicking force of amplitude f_0 in the membrane, which undergoes a normal displacement, δ (*lower*). In this case, the membrane experiences larger fluctuations of average amplitude $\Delta h + \delta$. To see this figure in color, go online.

via transmembrane- and membrane-associated proteins (47,48). To assemble the network, the distal tails of the spectrin filaments are connected at pinning nodes via junctional complexes consisting of actin, tropomyosin, protein band 4.1, and other regulatory proteins (Fig. 5 *A*, *inset*) (39,47,48). On average, at a given 4.1-based node, six spectrin ends make a reversible complex with each actin oligomer, producing an almost hexagonal network (39). Membrane attachment of the junctional nodes is provided by protein band 4.1 (49), which associates with spectrin/actin complexes, forming a high-affinity ternary complex that recognizes specific membrane pinning domains in the transmembrane protein glycophorin C (8,50,51). Ankyrin provides additional membrane linkage through spectrin association at a binding site located close to the filament midregion (52). This domain creates a tight linking association between spectrin and the cytoplasmic domain of protein band 3, the RBC anion exchanger (9). Network stability is mainly dependent on those two interactions, the one defined by the junctional complex at the distal ends of spectrin tetramers and the one defined by ankyrin (5). All the RBC cytoskeletal proteins except actin can be phosporylated by several kinases present in the erythrocyte (3–5). Regarding spectrin, an increased phosphorylation is known to decrease the mechanical stability of intact RBCs via cytoskeletal disentanglement (12). However, spectrin phosphorylation has been shown not to affect spectrin bound to ankyrin (3–5). The question then arises: how does ATP cause the dynamic remodeling of the cytoskeletal attachment? The answer should be puzzling, but some authors have plausibly argued in favor of ATP-dependent phosphorylation of the 4.1 protein (7,14), which controls the spectrin-membrane connections at the junctional nodes in the cytoskeletal network. Indeed, at a high level of phosphorylation, protein band 4.1 drastically reduces its ability to associate with spectrin, which triggers the dissociation of glycophorin C from the membrane skeleton (10,12,51,53). This phosphorylation is catalyzed by protein kinase C (PKC), which disassembles the spectrin/actin/4.1 trimer, the essential cytoskeletal complex that determines the mechanical stability of the RBC membrane (12). Indeed, PKC activation is known to lead to a decreased overall stability of the membrane skeleton (12,53,54), a structural effect that is consistent with a measurable increase of the dynamic fluctuations of the RBC membrane, as revealed by Betz et al. (7). Therefore, assuming the currently accepted mechanochemical model of the 4.1 nodes (51,53), every unpinning event bears a reaction kicking force that should be stressed on the lipid membrane upon dissociation of a spectrin filament from the junctional complex (14,26). The timescale involved in the unbinding process has not yet been determined, but our experiments suggest that the active shots last for ~0.1 s (see Fig. 3), in agreement with the active timescale detected by Betz et al. (7). The cartoon in Fig. 5 *B* depicts a generic kicking event where the active element of the membrane undergoes a net displacement, δ, occurring during time τ under a reaction force of amplitude f_0, exerted after unpinning phosphorylation at a junctional complex. In this model, a single-shot event is visualized as the net displacement, δ, of a membrane, which is driven by a kicking force of amplitude f_0. In view of the experimental data presented here, if the observed overcorrelation corresponds to the collective action of single kicking events of duration $\tau \approx 0.1$ s, assuming the active model of Fig. 5 *B*, on average, every elemental membrane patch undergoes a transverse displacement of length $\delta \approx \Delta h_h - \Delta h_f \approx 25$ nm, a distance compatible with the dimensions of the elemental cell of the cytoskeletal network (46).

Active forces driven by the RBC cytoskeleton dynamics

At every single cytoskeleton phosphorylation event, the membrane is reversibly pinched off from one pinning element, which individually exerts a kicking force of amplitude f_0 with a well-defined duration $\tau \approx 0.1$ s, which

determines the average burst time of the active component revealed in the correlation function; $\omega_{act} = \tau^{-1} \approx 10\ s^{-1}$ (Fig. 3 *B*). This characteristic time should define the frequency threshold to detect activity in the power spectrum. In native membranes, assuming that every skeletal unit cell contains only one potential kicker, the average surface density of active elements should be of the order $n_m \approx a^{-2} \approx 500$ kickers/μm^2. This estimation is compatible with the numerical density of membrane anchors (3). Therefore, assuming their homogeneous distribution along the cell with an average area of $A \approx 140\ \mu m^2$ (2,3), a maximal density of $n_m \leq 10^3\ \mu m^{-2}$ is calculated. It is noteworthy that the direct-force model in Eq. 8 (25,27) is able to describe the experimental PSDs of healthy cells taking the values $n_m(F/4\eta)^2 = 2.5 \times 10^5\ nm^2\ s^{-2}$ and $\tau = 0.1$ s. If these parameters are related to the structural model, and assuming a maximal areal density of potentially active elements (kickers) of $n_m \approx 5 \times 10^{-4}\ nm^{-2}$, one gets $F \approx 5 \times 10^{-4}$ pN (taking $\eta = 6$ cP). This value could become even higher if a lower density of membrane active sites is assumed at the equatorial cell site: $F \approx 2 \times 10^{-3}$ pN assuming $n_m \approx 2.5 \times 10^{-5}\ nm^{-2}$ (for $a \approx L \approx 200$ nm). Because $F \leq 2 \times 10^{-3}$ pN is the average force necessary to explain the additional power associated with the active motions of the healthy RBC flicker observed at large scales, only a small fraction (<10%) of spectrin-based cytoskeleton elements are required to be sparsely activated at a given time; since $F = p_{on} f_0$, assuming $f_0 \approx 5 \times 10^{-3}$ pN, one estimates $p_{on} \leq 0.1$, the probability for an active cytoskeletal node to be on at a given moment. For an individual kicker, the probability of being on is $p_{on} = \tau/(\Delta\tau + \tau)$, where $\Delta\tau$ is the waiting time between consecutive pulses of duration τ. Since $p_{on} \leq 0.1$, taking $\tau \approx 0.1$ s, we calculate a delay of $\Delta\tau \geq 1$ s as the time necessary for a single node in the cytoskeleton to reattach the spectrin filament and to exert a new kick on the membrane. The mechanical work associated with a single shot is $W_{shot} = f_0\delta \approx 1\ pN \times nm \approx k_BT$, just a fraction of the chemical energy released under the hydrolysis of one ATP molecule ($\Delta E_{ATP} \approx 13 k_BT$). In healthy cells, the ATP-induced dissociation of spectrin filaments is transient and reversible. A decreased activity is expected under the ATP-depletion condition, since the waiting time, $\Delta\tau$, for the forthcoming kicking event increases, thereby decreasing p_{on} and thus decreasing the strength of the effective force that produces the enhanced fluctuations. This is the case for drugged cells or after the use of KF. In the cross-linked cytoskeleton condition (glutaraldehyde treatment), no spectrin dissociation is possible ($p_{on} = 0$), and therefore a completely passive behavior is observed in the fixed RBCs. In healthy cells, every kicking event involves single pulses of amplitude $f_0 \approx 5 \times 10^{-3}$ pN sparsely applied during a short time, $\tau \approx 0.1$ s. Each cytoskeletal element that becomes active only sporadically ($p_{on} \leq 0.1$) is expected either to locally extend the membrane or to change curvature. To cause local membrane extension, a normal force of $f_\sigma \approx \sigma\delta \approx 5 \times 10^{-3}$ pN must be applied on its own cytoskeletal node ($\sigma_h \approx 0.2\ \mu$N/m). However, to produce a local change in membrane curvature, a larger force, of the order $f_\kappa \approx \kappa/\delta \approx 10$ pN (where $\kappa \approx \kappa_h \approx 65 k_BT$), has to be applied. Therefore, a single pulse exerting a direct force as low as $f_0 \approx 5 \times 10^{-3}$ pN would be able only to cause local membrane dilation, not change the local curvature, as deduced from the q-dependence of the active amplitudes (see Fig. 3 *D*). At a global scale, the action of $N_m = An_m \approx 10^5$ kickers working sparsely at a probability as low as $p_{on} \approx 0.1$ will produce a global force in the membrane of $F_{kick} = N_m^{1/2} f_0 p_{on} \approx 1$ pN. This force is enough to pump the breathing mode of the cytoskeleton network, $F_\kappa \approx \kappa/R \approx 0.1$ pN, and even to drive the large-wavelength tension modes involved in the global area dilation required for changing cell shape, $F_\sigma \approx \sigma R \approx 1$ pN. In healthy cells, in addition to the direct forces causing out-of-equilibrium activity at global scales (observed as enhanced low-q fluctuations), we detect a global membrane softening associated with ATP-dependent cytoskeletal activity. Although this mechanical softening could be merely compositional (due to cytoskeletal reorganization), membrane detachment is sparse and transient, which suggests a dynamical coupling between active forces and passive mechanical modes of the membrane. Bouvrais and colleagues reported a similar softening associated with the activity of pumping forces reconstituted in artificial bilayers devoid of a structural cytoskeleton (44), thus supporting the hypothesis of mechanical coupling rather than a pure compositional effect.

CONCLUSIONS

The results presented here represent an experimental proof of the existence of temporally correlated active forces exerted on the RBC membrane due to metabolic activity. Furthermore, these results strongly support the notion that such forces arise within the spectrin cytoskeleton. The active force appears as sporadic pulses of weak amplitude ($f_0 \approx 5 \times 10^{-3}$ pN) with a relatively long duration ($\tau \approx 0.1$ s). This kicking activity is spatially sparse over the cytoskeleton, but its dynamical correlation causes global effects on the cell membrane. This cytoskeletal force is shown to be metabolically driven (ATP-dependent) and to produce enhanced membrane fluctuations extending over large distances and relaxing over long times. Although the details of the dynamic mechanism of this activity in the RBC membrane remain unknown, our observations are compatible with the superposition of two stochastic motions that are different in nature, the active pulses due to cytoskeleton detachments and the mechanical modes driven by thermal motions. In healthy RBCs, spectrin detachment events are relatively infrequent and sparse, but sufficient to produce enhanced motions over cellular scales and overall mechanical softening. A more precise look at the constitutive relationships and the regulatory network of this cytoskeleton

force will allow for a detailed description of the active flicker mechanism and therefore a better understanding of the dynamic pathways underlying the active mechanics of RBCs in physiological conditions.

SUPPORTING MATERIAL

Supporting Materials and Methods and four figures are available at http://www.biophysj.org/biophysj/supplemental/S0006-3495(15)00489-0.

AUTHOR CONTRIBUTIONS

R.R.G. performed research, contributed analytic tools, analyzed the data, and discussed the results. I.L.M. contributed analytic tools, analyzed the data, and discussed the results. M.M. contributed analytic tools, analyzed the data, and discussed the results. G.E. discussed the results and wrote the article. N.S.G. and F.M. performed the research, contributed analytic tools, analyzed the data, discussed the results, and wrote the article.

ACKNOWLEDGMENTS

We are grateful to the Universidad Complutense de Madrid Medical Service (Medicina del Trabajo School of Medicine) for blood extractions.

This work was supported by grants FIS2009-14650-C02-01, FIS2012-35723, and CSD2007-0010 (Consolider-Ingenio Nanociencia Molecular) from the Ministerio de Economía y Competitividad (MINECO) and S2013/MIT-2807 (NanoBIOSOMA) and S2009MAT-1507 (NOBIMAT) from CAM to F.M.; and BFU2012-33932 from MINECO to G.E. N.S.G. gratefully acknowledges funding from the Israel Science Foundation (grant no. 580/12). R.R.G. was supported by the Formación de Personal Investigador program (MINECO). I.L.M. was supported by "Programa Ramon y Cajal" (RYC-2013-12609) from MINECO (Spain) and the European Research Council-European Union under grant ERC-StG-338133.

REFERENCES

1. Nakao, M., T. Nakao, and S. Yamazoe. 1960. Adenosine triphosphate and maintenance of shape of the human red cells. *Nature.* 187:945–946.
2. Alberts, B., A. Johnston, …, P. Walter. 2007. Molecular Biology of the Cell. Garland Science, New York.
3. Yawata, Y. 2004. Cell Membrane: The Red Blood Cell as a Model. Wiley-Blackwell, Hoboken, NJ, pp. 27–46.
4. Discher, D. E. 2000. New insights into erythrocyte membrane organization and microelasticity. *Curr. Opin. Hematol.* 7:117–122.
5. Mohandas, N., and P. G. Gallagher. 2008. Red cell membrane: past, present, and future. *Blood.* 112:3939–3948.
6. Park, Y., C. A. Best, …, M. S. Feld. 2010. Metabolic remodeling of the human red blood cell membrane. *Proc. Natl. Acad. Sci. USA.* 107:1289–1294.
7. Betz, T., M. Lenz, …, C. Sykes. 2009. ATP-dependent mechanics of red blood cells. *Proc. Natl. Acad. Sci. USA.* 106:15320–15325.
8. Bennett, V. 1990. Spectrin-based membrane skeleton: a multipotential adaptor between plasma membrane and cytoplasm. *Physiol. Rev.* 70:1029–1065.
9. Mohandas, N., and E. Evans. 1994. Mechanical properties of the red cell membrane in relation to molecular structure and genetic defects. *Annu. Rev. Biophys. Biomol. Struct.* 23:787–818.
10. Eder, P. S., C. J. Soong, and M. Tao. 1986. Phosphorylation reduces the affinity of protein 4.1 for spectrin. *Biochemistry.* 25:1764–1770.
11. Cianci, C. D., M. Giorgi, and J. S. Morrow. 1988. Phosphorylation of ankyrin down-regulates its cooperative interaction with spectrin and protein 3. *J. Cell. Biochem.* 37:301–315.
12. Manno, S., Y. Takakuwa, …, N. Mohandas. 1995. Modulation of erythrocyte membrane mechanical function by β-spectrin phosphorylation and dephosphorylation. *J. Biol. Chem.* 270:5659–5665.
13. Boal, D. H. 2002. Mechanics of the Cell. Cambridge University Press, Cambridge, United Kingdom.
14. Gov, N. S., and S. A. Safran. 2005. Red blood cell membrane fluctuations and shape controlled by ATP-induced cytoskeletal defects. *Biophys. J.* 88:1859–1874.
15. Blowers, R., E. M. Clarkson, and M. Maizels. 1951. Flicker phenomenon in human erythrocytes. *J. Physiol.* 113:228–239.
16. Brochard, F., and J. F. Lennon. 1975. Frequency spectrum of the flicker phenomenon in erythrocytes. *J. Phys.* (*France*). 36:1035–1047.
17. Tuvia, S., A. Almagor, …, S. Yedgar. 1997. Cell membrane fluctuations are regulated by medium macroviscosity: evidence for a metabolic driving force. *Proc. Natl. Acad. Sci. USA.* 94:5045–5049.
18. Tuvia, S., S. Levin, …, R. Korenstein. 1998. Mechanical fluctuations of the membrane-skeleton are dependent on F-actin ATPase in human erythrocytes. *J. Cell Biol.* 141:1551–1561.
19. Strey, H., M. Peterson, and E. Sackmann. 1995. Measurement of erythrocyte membrane elasticity by flicker eigenmode decomposition. *Biophys. J.* 69:478–488.
20. Evans, J., W. Gratzer, …, J. Sleep. 2008. Fluctuations of the red blood cell membrane: relation to mechanical properties and lack of ATP dependence. *Biophys. J.* 94:4134–4144.
21. Puckeridge, M., and P. W. Kuchel. 2014. Membrane flickering of the human erythrocyte: constrained random walk used with Bayesian analysis. *Eur. Biophys. J.* 43:157–167.
22. Yoon, Y. Z., H. Hong, …, P. Cicuta. 2009. Flickering analysis of erythrocyte mechanical properties: dependence on oxygenation level, cell shape, and hydration level. *Biophys. J.* 97:1606–1615.
23. Park, Y., C. A. Best, …, G. Popescu. 2010. Measurement of red blood cell mechanics during morphological changes. *Proc. Natl. Acad. Sci. USA.* 107:6731–6736.
24. Yoon, Y. Z., J. Kotar, …, P. Cicuta. 2011. Red blood cell dynamics: from spontaneous fluctuations to non-linear response. *Soft Matter.* 7:2042–2051.
25. Lin, L. C., N. Gov, and F. L. Brown. 2006. Nonequilibrium membrane fluctuations driven by active proteins. *J. Chem. Phys.* 124:74903.
26. Gov, N. S. 2007. Active elastic network: cytoskeleton of the red blood cell. *Phys. Rev. E Stat. Nonlin. Soft Matter Phys.* 75:011921.
27. Ben-Isaac, E., Y. Park, …, Y. Shokef. 2011. Effective temperature of red-blood-cell membrane fluctuations. *Phys. Rev. Lett.* 106:238103.
28. Rodríguez-García, R., M. Mell, …, F. Monroy. 2011. Subdiffusive fluctuation dynamics of rigid membranes as resolved by ultrafast videomicroscopy. *Europhys. Lett.* 94:28009.
29. Faucon, J. F., M. D. Mitov, …, P. Bothorel. 1989. Bending elasticity and thermal fluctuations of lipid membranes. Theoretical and experimental requirements. *J. Phys.* (*France*). 50:2389–2414.
30. Pecreaux, J., H. G. Dobereiner, …, P. Bassereau. 2004. Refined contour analysis of giant unilamellar vesicles. *Eur. Phys. J. E Soft Matter.* 13:277–290.
31. Plishker, G. A. 1985. Iodoacetic acid inhibition of calcium-dependent potassium efflux in red blood cells. *Am. J. Physiol.* 248:C419–C424.
32. Tsukita, S., S. Tsukita, …, M. Nakao. 1981. Electron microscopic study of reassociation of spectrin and actin with the human erythrocyte membrane. *J. Cell Biol.* 90:70–77.
33. Brown, J. N. 1975. The avian erythrocyte: a study of fixation for electron microscopy. *J. Microsc.* 104:293–305.
34. Gumińska, M., and J. Sterkowicz. 1976. Effect of sodium fluoride on glycolysis in human erythrocytes and Ehrlich ascites tumour cells in vitro. *Acta Biochim. Pol.* 23:285–291.

35. Milner, S. T., and S. A. Safran. 1987. Dynamical fluctuations of droplet microemulsions and vesicles. *Phys. Rev. A.* 36:4371–4379.

36. Deuling, H. J., and W. Helfrich. 1976. Red blood cell shapes as explained on the basis of curvature elasticity. *Biophys. J.* 16:861–868.

37. Zeman, K., H. Engelhard, and E. Sackmann. 1990. Bending undulations and elasticity of the erythrocyte membrane: effects of cell shape and membrane organization. *Eur. Biophys. J.* 18:203–219.

38. Gov, N. 2004. Membrane undulations driven by force fluctuations of active proteins. *Phys. Rev. Lett.* 93:268104.

39. Liu, S. C., L. H. Derick, and J. Palek. 1987. Visualization of the hexagonal lattice in the erythrocyte membrane skeleton. *J. Cell Biol.* 104:527–536.

40. Li, J., G. Lykotrafitis, …, S. Suresh. 2007. Cytoskeletal dynamics of human erythrocyte. *Proc. Natl. Acad. Sci. USA.* 104:4937–4942.

41. Feig, S. A., S. B. Shohet, and D. G. Nathan. 1971. Energy metabolism in human erythrocytes. I. Effects of sodium fluoride. *J. Clin. Invest.* 50:1731–1737.

42. Camley, B. A., and F. L. Brown. 2011. Beyond the creeping viscous flow limit for lipid bilayer membranes: theory of single-particle microrheology, domain flicker spectroscopy, and long-time tails. *Phys. Rev. E Stat. Nonlin. Soft Matter Phys.* 84:021904.

43. Cokelet, G. R., and H. J. Meiselman. 1968. Rheological comparison of hemoglobin solutions and erythrocyte suspensions. *Science.* 162:275–277.

44. Bouvrais, H., F. Cornelius, …, O. G. Mouritsen. 2012. Intrinsic reaction-cycle time scale of Na^+,K^+-ATPase manifests itself in the lipid-protein interactions of nonequilibrium membranes. *Proc. Natl. Acad. Sci. USA.* 109:18442–18446.

45. Nans, A., N. Mohandas, and D. L. Stokes. 2011. Native ultrastructure of the red cell cytoskeleton by cryo-electron tomography. *Biophys. J.* 101:2341–2350.

46. Liu, F., J. Burgess, …, A. Ostafin. 2003. Sample preparation and imaging of erythrocyte cytoskeleton with the atomic force microscopy. *Cell Biochem. Biophys.* 38:251–270.

47. Byers, T. J., and D. Branton. 1985. Visualization of the protein associations in the erythrocyte membrane skeleton. *Proc. Natl. Acad. Sci. USA.* 82:6153–6157.

48. Shen, B. W., R. Josephs, and T. L. Steck. 1986. Ultrastructure of the intact skeleton of the human erythrocyte membrane. *J. Cell Biol.* 102:997–1006.

49. Conboy, J. G. 1993. Structure, function, and molecular genetics of erythroid membrane skeletal protein 4.1 in normal and abnormal red blood cells. *Semin. Hematol.* 30:58–73.

50. Bennett, V. 1989. The spectrin-actin junction of erythrocyte membrane skeletons. *Biochim. Biophys. Acta.* 988:107–121.

51. Discher, D. E., R. Winardi, …, N. Mohandas. 1995. Mechanochemistry of protein 4.1's spectrin-actin-binding domain: ternary complex interactions, membrane binding, network integration, structural strengthening. *J. Cell Biol.* 130:897–907.

52. Davis, L. H., and V. Bennett. 1990. Mapping the binding sites of human erythrocyte ankyrin for the anion exchanger and spectrin. *J. Biol. Chem.* 265:10589–10596.

53. Manno, S., Y. Takakuwa, and N. Mohandas. 2005. Modulation of erythrocyte membrane mechanical function by protein 4.1 phosphorylation. *J. Biol. Chem.* 280:7581–7587.

54. de Oliveira, S., A. S. Silva-Herdade, and C. Saldanha. 2008. Modulation of erythrocyte deformability by PKC activity. *Clin. Hemorheol. Microcirc.* 39:363–373.

Supplementary Information

Direct cytoskeleton forces cause membrane softening in red blood cells

Ruddi Rodríguez-García[1], Iván López-Montero[1,2], Michael Mell[1,2], Gustavo Egea[3], Nir S. Gov[4] and Francisco Monroy[1,2,*]

[1]Department of Physical Chemistry, Universidad Complutense. Ciudad Universitaria s/n 28040 Madrid, Spain.
[2]Instituto de Investigación Hospital Doce de Octubre (i+12). Avenida de Córdoba, s/n 28041 Madrid, Spain.
[3]Departament of Cell Biology, Immunology and Neurosciences, University of Barcelona, School of Medicine and Instituts d'Investigacions Biomèdiques August Pi i Sunyer (IDIBAPS) and Nanociències i Nanotecnologia (IN^{2}UB), 08036 Barcelona, Spain.
[4]Department of Chemical Physics, Weizmann Institute of Science. Rehovot 76100, Israel.

SI1. Thermal fluctuations of quasi-spherical vesicles

a) Bending modes in the spherical harmonic base: quasi-spherical spectrum. Currently the only membrane geometry whose flickering spectrum can be solved in a purely analytical way is the quasi-spherical vesicle (1). The fluctuating vesicle is assumed with a time-averaged spherical shape with volume and area being conserved quantities. Under this assumption, Milner and Safran considered the fluctuations of a spherical membrane with bending energy given by the Helfrich expression (2):

$$F_{bend} = \frac{1}{2}\kappa \int_S \left(c - c_0\right)^2 dA \qquad \text{(S1.1)}$$

where κ is the bending modulus of the membrane, $c = 1/r_1 + 1/r_2$, the local value of the mean curvature which is defined by two principal radii of curvature and c_0 the spontaneous curvature.

In spherical coordinates, with origin in the centre of the vesicle, assuming the quasi-spherical approach the local radius of the deformed vesicle can be expressed as:

$$r\left(\theta,\varphi,t\right) = R + h\left(\theta,\varphi,t\right) \qquad \text{(S1.2)}$$

where R is the average spherical radius and h the normal displacement.

Since the change in curvature depends only on the normal displacement, h is chosen to express the local curvature and its relative value expanded in spherical harmonics (SH-base):

$$\frac{h(\theta,\varphi,t)}{R}=\sum_{l=m}^{l_{\max}}\sum_{m=2}^{l}U_{lm}(t)Y_{lm}(\theta,\varphi) \qquad \text{(S1.3)}$$

with dimensionless amplitudes $U_{lm}(t)$ given for the SHs defined for the discrete values of the azimuthal (m) and polar (l) integer numbers. The sum starts from $l = m = 2$ because the fundamental swelling mode $l = m = 0$ does not conserve volume and $l = m = 1$ represents a uniform displacement of the center of mass of the entire sphere.

Using this solution, the bending energy in Eq. (S1.1) is minimized with the constraint of constant area, which is treated introducing the membrane tension $\sigma(\Delta)$ as a Lagrange multiplier (2). Within the harmonic approximation for the fluctuation energy, after applying the equipartition theorem for the amplitudes U_{lm}, their quadratic time-averages are obtained as (2):

$$\left\langle U_{lm}^2\right\rangle=\frac{k_BT}{\kappa}\frac{1}{(l+2)(l-1)\left[l(l+1)+\Sigma\right]} \quad \textit{for} \quad l\geq 2, \qquad \text{(S1.4)}$$

with the dimensionless parameter:

$$\Sigma=\frac{\sigma(\Delta)R^2}{\kappa}+4c_0R-2c_0^2R^2 \qquad \text{(S1.5)}$$

accounting for an effective tension that depends of the excess area (Δ) and of the local spontaneous curvature (2). The amplitudes in Eq. (S1.4) represents the quadratic coefficients of the discrete expansion in Eq. (S1.3) using the HS base.

Every spherical harmonics can be viewed as a normal mode of membrane fluctuation in the quasi-spherical object, the 2D-fluctuation geometry of every discrete mode being defined by the degree l and the order m (azimuthal) of the corresponding spherical harmonic. In practice, what is seen under the optical microscope in a flickering experiment is the equatorial cross section of a quasi-spherical membrane. Consequently, only the normal displacements $h(\theta=\pi/2, \varphi, t)$ are measurable along the equatorial contour defined by the variation range of the azimuthal angle $\varphi \in [0, 2\pi]$. As far the quasi-spherical approach is assumed (only one radius defines the average profile), the normal equatorial displacements, in Fourier space, are given by:

$$h(q_m,t)=\frac{1}{2\pi}\int_0^{2\pi}h(\pi/2,\varphi,t)e^{-im\varphi}d\varphi \qquad \text{(S1.6)}$$

with $m = 2, 3, \ldots$) representing the discrete values of the azimuthal number describing the allowed undulations in the circular equator; the discrete wavelengths $\lambda_m = 2\pi R/m$, thus $q_m = 2\pi/\lambda_m = m/R$.

From the expansion in Eq. (S1.3), using the SH base, for a given equatorial mode Eq. (S1.6) re-writes as:

$$h(q_m,t) = \frac{R}{2\pi}\sum_{l=m}^{l_{\max}}\left[U_{lm}(t)\int_0^{2\pi} Y_{lm}(\pi/2,\varphi)e^{-im\varphi}d\varphi\right] \tag{S1.8}$$

where l_{max} is the cut-off number characterizing the fluctuation mode of the shortest possible wavelength. Its order is given by the bilayer thickness, $d \approx 5$nm, thus $l_{max} \approx q_{max} R \approx 2\pi R/d \approx 10^3$.

The amplitude of the equatorial modes can be expressed as a sum of the equatorial projection ($\theta = \pi/2$) of the spherical harmonics over the possible states of polar orientations with wavelengths compatible with the equatorial undulation, *i.e.* with $l \geq m$.

b) Autocorrelation function. In the intent to describe fluctuation dynamics of quasi-spherical membranes to obtain the autocorrelation function (*ACF*), MS considered linear response together with the fluctuation-dissipation theorem and obtained the height-to-height correlations as a progressive sum of exponential decays corresponding to the different spherical harmonics (2). When particularized to the equatorial fluctuations, for the *ACF* one gets:

$$ACF = \langle h(q_m,0)h(q_m,t)\rangle = R^2\sum_{l=m}^{l_{\max}}\langle U_{lm}^2\rangle\, e^{-\omega_l t} \tag{S1.9}$$

where the square amplitude of the *m*-equatorial mode is given by Eq. S1.4 (3,4), and the relaxation frequencies of the discrete modes are given by (1,2):

$$\omega_l(q) = \frac{\kappa}{\eta R^3}\frac{l(l+1)+\Sigma}{Z(l)}, \tag{S1.10a}$$

where *Z(l)* is a geometrical factor given by:

$$Z(l) = \frac{(2l+1)(2l^2+2l-1)}{l(l+1)(l+2)(l-1)} \tag{S1.11}$$

The above formulas describe discrete modes in the quasi-spherical geometry. This imposes periodical boundary conditions which make emerge the quantization rules intrinsic to the spherical harmonics base. However, in the limit of small curvature ($R \to \infty$), the characteristics of the spherical modes would coincide with solutions in a planar membrane. Indeed, in the limit of high wavevectors (high l, $q \approx l/R$), one has $Z(l) \approx 4/l$ so, in the absence of spontaneous curvature ($c_0 = 0$), the relaxation rates in Eq. (S1.10a) should be found to vary following the approximate formula:

$$\omega_q \approx \frac{\kappa q^3 + \sigma q}{4\eta} \qquad \text{(S1.10b)}$$

which coincides with the well-known expression for the relaxation rate of the bending/tension mode in a planar membrane (5).

This corresponds to a planar mode of wavevector q with elastic energy $F_q \approx \sigma q^2 + \kappa q^4$ (taking Eq. S1.4 in the high-l limit, where $l \approx q/R$), which dissipates energy by viscous friction with the bulk fluid. For a liquid of viscosity η, considering the usual expression of the bulk Oseen tensor; in Fourier space (6):

$$\Lambda_q = \frac{1}{4\eta q} \qquad \text{(S1. 12)}$$

Solving the stochastic equation of motion for the thermal modes of a flexible membrane in a pure viscous fluid (7) (ξ_q is the stochastic field describing a thermal white noise):

$$\frac{\partial h_q}{\partial t} = -E_q \Lambda_q h_q + \Lambda_q \xi_q \qquad \text{(S1.13)}$$

one recovers the relaxation rate in Eq. (S1.10b) as:

$$\omega_q = \Lambda_q E_q = \frac{\sigma q^2 + \kappa q^4}{4\eta q} = \frac{\sigma q + \kappa q^3}{4\eta} \qquad \text{(S1.10b)bis}$$

SI2. Autocorrelation function of the equatorial modes

SI2.a) Fluid membrane vesicles fluctuating in a viscous fluid. In a typical flickering experiment one detects radial deflections in the equatorial plane, which are described as

quadratic amplitudes of the equatorial modes; in terms of the SH base, each equatorial fluctuation characterized by an azimuthal wavevector q_m (= R/m) is described by the discrete sum defined in Eq. (S1.9). The key point is that the dynamic correlations are given by an infinite sum of harmonic contributions projected in the equator, where the summation starts with a fundamental spherical harmonic of equal wavevector than the considered equatorial mode, *i.e.* $l_0 = m$. For pure bending modes ($\sigma \approx 0$; neglecting the spontaneous curvature, $c_0 = 0$ thus $\Sigma \approx 0$), in the continuous approximation*, Eq. (S1.9) can be re-written in the integral form:

$$\left\langle h(q,0)h(q,t)\right\rangle_{bend} \approx R^2 \frac{k_B T}{\kappa} \int_q^\infty \frac{\exp\left[-\left(\kappa q^3/4\eta\right)t\right]}{q^4 R^4} R dq \tag{S2.1}$$

with $dm = R\,dq$.

To perform integration, we consider the change of variable:

$$\begin{aligned} \left(\kappa q^3/4\eta\right)t = \omega_q t = z^3 \\ q\left(\kappa t/4\eta\right)^{1/3} = z \end{aligned} \quad \Rightarrow \quad dq = \left(\kappa t/4\eta\right)^{-1/3} dz \tag{S2.2}$$

Then, Eq. (S2.2) can be rewritten with the simplified form:

$$\left\langle h(q,0)h(q,t)\right\rangle_{bend} \approx \frac{1}{R}\frac{k_B T}{\kappa q^3}\left(\omega_q t\right)\int_z^\infty \frac{e^{-z^3}}{z^4} dz \tag{S2.3}$$

and performing the integration:

$$\int_z^\infty \frac{e^{-z^3}}{z^4} dz = -\left[\frac{e^{-z^3}}{3z^3} - \frac{\mathrm{E}_1\left(z^3\right)}{3}\right]_z^\infty \tag{S2.4a}$$

with the special function $\mathrm{E}_1(x)$ defined as:

$$\mathrm{E}_1(x) = \int_x^\infty \frac{e^{-u}}{u} du\,, \tag{S2.5}$$

* In the continuous approximation to Eq. (S1.9), the integration is performed as the continuous summation under all the possible values of l (= qR), taking now q as a continuous variable instead of the discrete variable l. The integration in Eq. (S2.1) is performed over the "continuous" l, with the differential element being $dl = Rdq$.

which takes the limiting value $E_1(\infty) = 0$; consequently, the integral in Eq. (S2.4a) rewrites as:

$$\int_z^\infty \frac{e^{-z^3}}{z^4}\,dz = \frac{e^{-z^3}}{3z^3} - \frac{\mathrm{E}_1\left(z^3\right)}{3} = \frac{1}{3}\left[\frac{e^{-\omega_q t}}{\omega_q t} - \mathrm{E}_1\left(\omega_q t\right)\right] \tag{S2.4b}$$

Finally, substituting Eq. (S2.4b) in Eq. (S2.3), one finds:

$$\left\langle h(q,0)h(q,t)\right\rangle_{bend} \approx \frac{1}{3R}\frac{k_B T}{\kappa q^3}\left[e^{-\omega_q t} - \left(\omega_q t\right)\mathrm{E}_1\left(\omega_q t\right)\right] \tag{S2.6}$$

The expression in Eq. (S2.6) defines bending-dominated correlations as an exponential decay corrected by the sharply decaying function $E_1(x)$ (see Fig. S1.A). If bending-dominated, the amplitude of the equatorial modes is expected with an effective $\langle h_{eq}^2\rangle_{bend} \approx (1/3R)\, k_B T/\kappa q^3$ dependence, in agreement with the calculation performed by Pécreaux et al. (4) for the 1D-projection of the rms amplitude of the surface modes projected on the equatorial circumference. Similarly, if membrane tension dominates ($\sigma R^2 >> \kappa$), in the continuous limit Eq. (S2.1) can be expressed as:

$$\left\langle h(q,0)h(q,t)\right\rangle_{tens} \approx \frac{k_B T}{\sigma}\int_q^\infty \frac{\exp\left[-\left(\sigma q/4\eta\right)t\right]}{q^2 R^2}\,R dq\,, \tag{S2.7}$$

which, following the same integration schema as above, can be finally written as:

$$\left\langle h(q,0)h(q,t)\right\rangle_{tens} \approx \frac{1}{R}\frac{k_B T}{\sigma q}\left[e^{-\omega_q t} - \left(\omega_q t\right)\mathrm{E}_1\left(\omega_q t\right)\right] \tag{S2.8}$$

This expression for the correlation function of the tension mode exhibits the same time-dependence as Eq. (S2.6), the corresponding function for bending-dominated modes. However, the equatorial amplitude varies as $\langle h_{eq}^2\rangle_{tens} \approx (1/R)\, k_B T/\kappa q$, as predicted by Pécreaux et al. (4). To understand the time dependences in Eqs. (S2.6/S2.8) –which are similar in the two different cases (bending/tension modes with bulk friction), the mother expression in Eq. (S2.1) teaches that, when detected at the equatorial plane, the time autocorrelation function (*ACF*) actually corresponds to a summation over all the relaxations existing in the spherical modes that are congruent ($l \geq m$) with the equatorial undulation (characterised by $q_m = m/R$). The sum in Eq. (S2.1) actually superposes a number of exponential decays corresponding to the different *l*-modes projected over the equatorial plane, thus the time dependence of the *ACF* cannot be obtained in a closed

form. From the characteristics of the tension/bending modes in fluctuating membranes with bulk friction, two important properties are deduced for the successive off-plane modes that contribute to a given equatorial undulation: a) they contribute with a decaying amplitude, b) they relax at an increasingly faster rate. Consequently, relaxation of a given equatorial mode (m) should be chiefly dominated by the rate of the master spherical harmonic ($l = m$) with minor contributions from (weaker and faster) higher harmonics ($l > m$). In the case of an incompressible fluid membrane, the relaxation of the equatorial fluctuations in vesicles is described by a time-decay of the functional form:

$$ACF_{tens/bend}^{(eq)} \approx e^{-\omega_q t} - \left(\omega_q t\right) \mathrm{E}_1\left(\omega_q t\right), \qquad \text{(S2.6/S2.8)bis}$$

which is common to modes of the two classes, tension/bending modes with a dissipation due to bulk friction (see Fig. S1A).

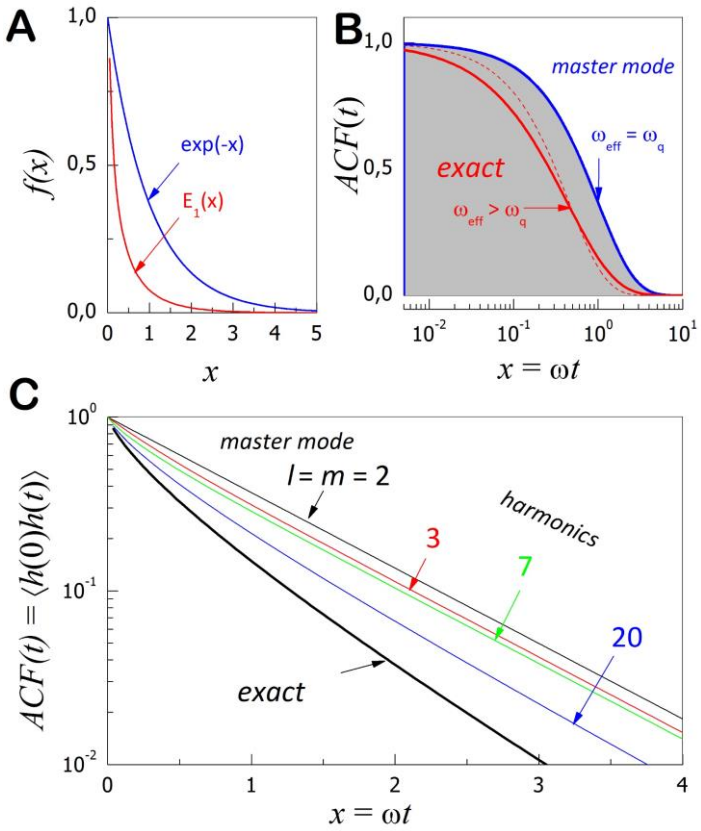

Fig. S1. A) Functional dependence of the relaxation profile of a single spherical mode, (—) f(x) ~ exp(-x), and the summation function accounting from its harmonics, (—) f(x) ~ $E_1(x)$. **B)** ACF-single-exponential master decay of a given equatorial mode (—), compared with its actual relaxation (—), which is a faster with a non-exponential profile affected by all of their higher harmonics present in the grey zone. (- - -) Single exponential of equivalent relaxation time, $\omega_{eff} \approx 1.30\ \omega_q$. **C)** Comparison between the exact solution in Eqs. (S2.6)/(S2.8) for the time dependence of the ACF of equatorial fluctuations in vesicles and the approximate solution to Eq. (S2.1) as truncated series.

The first term of this function corresponds to the master relaxation of the fundamental contribution ($l = m$) to the equatorial mode with $q = m/R$ and relaxation rate ω_q given by Eqs. (S1.12). The second term, which takes-off the exponential decay making it faster, arises from the weighted summation over the higher harmonics ($l > m$). Such contributions give rise to a slight increase of the phenomenological relaxation rates up to an effective value faster than the one expected for the master mode ω_q (see Fig. S1B). This cumulative effect of the higher harmonics was previously discussed by Yoon et al. (8) in the context of RBC flickering, although no analytic solution was explicitly calculated. From the numerical analysis of the cumulative *ACF*, those authors proposed a global relaxation interpolated by a single exponential profile, $ACF(t) \sim \exp[-\omega_q^{(eff)}t]$ with an effective decay rate, $\omega_q^{(eff)} \approx 1.30\ \omega_q$, faster than the master mode (8) (see Fig. SB). However, such a single exponential approximation, albeit successful in describing the relaxation rates, it provides a quite poor description of the exact shape of the cumulative relaxation profile (see Fig. S1B). The multimodal relaxation intrinsic to the observation of the equatorial modes produces a cumulative effect, i.e. the progressively smaller contribution of the faster harmonics at shorter times. In practice, such a heterogeneous relaxation could be accounted for by phenomenological functions, like a "stretched exponential" profile. However, since analytic solutions are available for bending- and tension-governed equatorial fluctuations in vesicles, the experimental *ACF*s should be fitted to the physically significant functions in Eqs. (S2.6) and (S2.8), respectively.

SI2.b) Thermal fluctuations of the RBC membrane. The RBC membrane is significantly more complex than the lipid bilayer in a vesicle. The first theoretical studies emphasized on the global bending stiffness and the bulk viscosity as the two only relevant parameters to explain RBC fluctuations (9,10). The first as the only restoring force exerted by the membrane upon a shape fluctuation. The second as the only viscous parameter relevant to account for frictional dissipation. Obviously, possible intrinsic effects arising from the internal structure of the RBC membrane were almost missed in those models. In the case of RBCs, an underlying cytoskeleton is reinforcing the lipid bilayer, thus shear elasticity must be added as an additional restoring force as well. Furthermore, the coupling between membrane and cytoskeleton must be additionally considered as a confinement contribution which contributes to increase the local value of

the membrane elastic energy upon separating the bilayer from the cytoskeleton. Therefore, the landscape is significantly more complex in RBCs than in bilayer vesicles, so a progressive approximation to the complete physical problem is required, first, considering the indispensable ingredients in a minimal model.

Static spectrum: Planar membrane approximation. In the approximate planar-membrane description, which is exact at high wavevectors, the elastic free energy for a RBC membrane is the sum of the usual Canham-Helfrich Hamiltonian with isotropic bending and tension elastic components describing the elasticity of the fluid membrane plus new terms accounting for the additional contributions of the cytoskeleton, namely, a shear component due to in-plane rigidity and a confinement term, these are:

$$F_{RBC} \approx \frac{1}{2}\left[\sigma\left(\nabla h\right)^2 + \kappa\left(\nabla^2 h\right)^2\right] + \mu\left[2\left(\frac{\partial^2 h}{\partial x \partial y}\right)^2 + \frac{1}{2}\left(\frac{\partial^2 h}{\partial x^2} - \frac{\partial^2 h}{\partial y^2}\right)^2\right] + \frac{1}{2}\gamma h^2 \quad \text{(S2.9)}$$

where the planar strain field (h) is defined as the changes in membrane height with respect to the unstressed reference state in which the membrane is assumed in the flat configuration.

The presence of a rigid cytoskeleton introduces two additional internal components to the elastic response in Eq. (S2.9): **1) in-plane shear**, characterized by a shear modulus (μ) (11) and **2) cytoskeleton confinement**, which makes the free energy to increase with increasing the separation between the membrane and the cytoskeleton (described as a harmonic potential characterized by a spring constant (γ) (12). Since all these new harmonic contributions to the elastic Hamiltonian are summative, in Fourier-space, they contribute altogether as cumulative summands to the effective restoring force. Therefore, similarly to the case of thermal fluctuations in a fluid membrane, considering equipartition of the thermal energy in the different thermal modes, in the planar membrane approximation the spectral amplitudes write as (11,12):

$$\left\langle h_q^2 \right\rangle \approx \frac{k_B T}{\sigma q^2 + \kappa_{eff}\left(q\right) q^4} \quad \text{(S2.10)}$$

with a q-dependent effective bending constant (11):

$$\kappa_{eff}\left(q\right) = \kappa + \frac{9 k_B T}{16\pi\kappa}\mu q^{-2} + \gamma q^{-4} \quad \text{(S2.11)}$$

where the shear contribution is considered in the regime of intermediate q's, where shear modes are effectively decoupled of bending modes (13). In that regime, differently to bending modes whose energy varies as $F_{bend} \sim \kappa q^4$, the energy of the shear contribution goes as $F_{shear} \sim \mu q^2$, similarly to the q-dependence assumed by Sackmann and cols (16) and Brochard and Lennon (14) for the contribution of shear rigidity to the RBC flicker.

Static spectrum: Equatorial fluctuations in the quasi-spherical approximation. Following the seminal work by Brochard and Lennon (14), we will take the sphere as the reference state to describe the equatorial fluctuations of the RBC flicker. Although this is of course only an approximation, it is however adequate to resolve the variational problem of the free energy minimization with a reasonable spherical harmonic base and well adapted to the circular symmetry of the equatorial fluctuations. Therefore, when applied to describe the RBC discocyte, the calculated elastic moduli must be considered as apparent values (not absolute) referred to the hypothetical spherical reference. This consideration was early pointed out by Brochard and Lennon (14), who considered this a reasonable approximation to the RBC flicker. Following the MS description for the bending fluctuations of spherical vesicles and droplets, Faucon et al. (3) discussed the

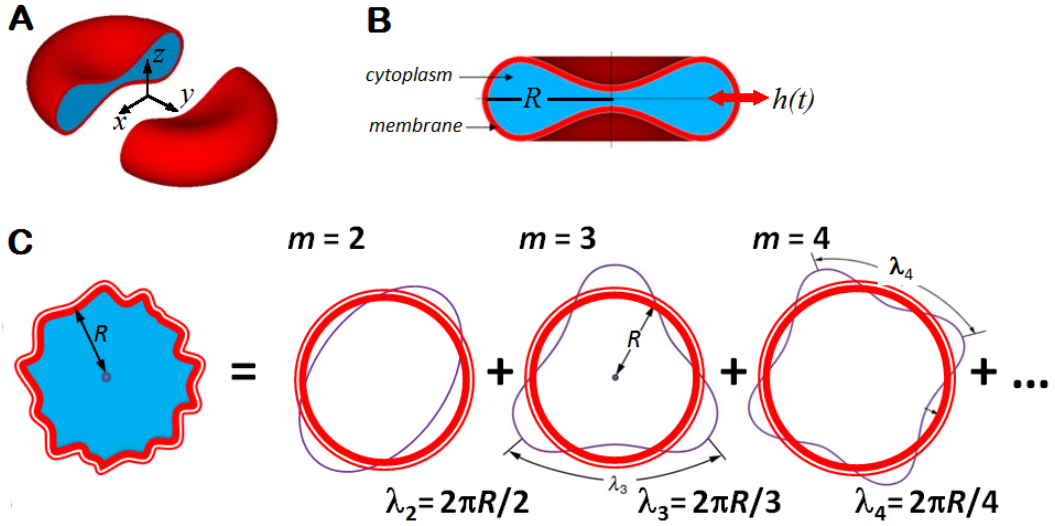

Fig. S2. A) Coordinate system for the quasi-spherical description of the discocyte geometry. **B)** Equatorial geometry: The equatorial modes of fluctuation are described as one-dimensional displacements h(t) with respect to the average radius measured at the equatorial emplacement. **C)** Discrete mode decomposition of the equatorial fluctuations. The equatorial modes are described as the discrete eigen-modes in the circular orbit with wavelengths $\lambda_m = 2\pi R/m$ obtained as integer submultiple of the elemental length $2\pi R$. In the spherical harmonics decomposition, these equatorial eigen-modes correspond to the different values of the azimuthal number m.

limitations of the quasi-spherical method to describe the equatorial flickering of non-

spherical vesicles (see Fig. S2). In practice, one could use the MS expressions with apparent values of the two main mechanical parameters (κ and σ), which must be affected by the other intrinsic characteristics of the membrane due to the presence of the cytoskeleton. Faucon et al. (3) demonstrated that an approximate description of the flickering fluctuations as Fourier modes describes quite accurately the exact MS equations for the quasi-spherical case. So, the quasi-spherical modes with azimuthal wavelength $\lambda_m = 2\pi R/m$ at the equatorial emplacement of average radius R, practically coincide with a Fourier modes of wavenumber $q_m = 2\pi/\lambda_m = m/R$. For $m \geq 5$, they differ very little (by less than the experimental error), which justifies using the much simpler solutions in Eq. (S2.10-S2.11) with the exact MS equations (2). In the quasi-spherical approach to the RBC flicker the equatorial fluctuations are described as a discrete set of spherical harmonics with polar axis parallel to the symmetry normal axis of the discoid cell (15,16). At this quasi-spherical emplacement, the spectrum of the discrete normal modes is given by (2,17):

$$P_m\left(q = m/R\right) = \frac{k_B T}{\kappa_{eff}\left(q\right)} \sum_{l=m} \left\{ \left(l+1\right)\left(l-1\right)\left[l\left(l+1\right) + \Sigma_{eff} \right] \right\}^{-1} \qquad \text{(S2.12)}$$

with effective parameters $\kappa_{eff}(q)$ given by Eq. (S2.11) and Σ_{eff} by Eq. (S1.5). Here, the membrane tension can be effectively reduced by the amount of excess area (Δ). Deviations from the equilibrium curvature should also contribute to create effective surface area eventually increasing fluctuations; in the MS theory this effect is accounted for the curvature parameter c_0 ($c_0 = -2.4$ for the RBC-discocyte shape) (9).

Autocorrelation function. Fluid lipid bilayers in model membranes are usually considered to dynamically behave as an incompressible fluid without internal dissipation. However, the lipid bilayer of real cell membranes is composed by a crowded mixture of lipids and proteins, a molecularly heterogeneous system which is expected with a

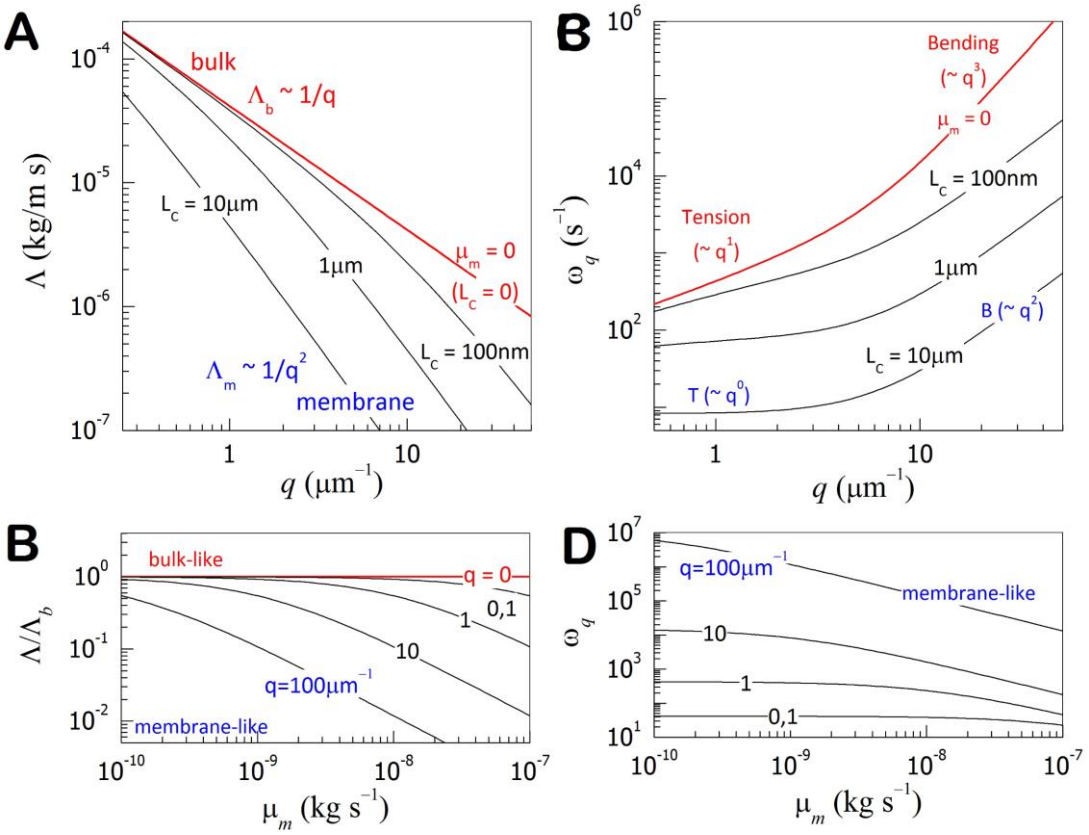

Fig. S3. A) Hydrodynamic compliance as a function of the wavevector. For ideal fluid membrane (zero membrane viscosity, $\mu_m = 0$), one expects a monotonic q-dependence $\Lambda_{bulk} = 1/4\eta q$. As the membrane viscosity increases, also the characteristic length does, $L_C = \mu_m/2\eta$, so one finds renormalization to membrane dominated frictional regime at progressively lower wavevectors, $\Lambda_{memb} \approx 1/2\mu_m q^2$. **B)** Decrease of the hydrodynamic compliance with membrane viscosity. The relative value of the Oseen tensor (with respect to the bulk value) decreases with μ_m, the decrease being progressively faster at higher q. **C)** Dispersion of the tension/bending mode in a membrane with variable membrane viscosity. The typical crossover between tension-like ($\omega_q \sim q$) and bending-dominated ($\omega_q \sim q^3$) modes in a fluid membrane is only observed with zero membrane viscosity ($\mu_m = 0$). The increase of membrane viscosity causes: 1) an absolute decrease of the relaxation rates, 2) a displacement of the tension/bending crossover at smaller wavevectors, and 3) an overall change of the dispersion behavior characterized by a decrease of the dispersion exponents; in the limit of high membrane viscosity ($\mu_m >> 2\eta/q$ or $qL_c >> 1$), the tension mode renormalize to a non-dispersive behavior, $\omega_q \approx \sigma q^0/2\mu_m$, and the bending mode to the membrane-dominated frictional dependence $\omega_q^{(memb)} \approx \kappa q^2/2\mu_m$, comparatively weaker than the bulk-dominated dispersion $\omega_q^{(bulk)} \approx \kappa q^3/4\eta$. **D)** Dependence with membrane viscosity of the relaxation rates of the tension/bending mode. At low wavevectors ($qL_c << 1$), a crossover between a μ_m-independent bulk-like regime and a membrane-like regime is observed. At wavevectors high enough, a monotonous membrane-dominated regime is expected.

comparatively higher intrinsic viscosity than single lipid bilayers. Consequently, significant contributions to frictional dissipation are expected from the internal viscosity of the RBC membrane. Many theoretical works have addressed the hydrodynamics of viscous membranes in the linear flow regime (18,19). In addition to the usual bulk friction accounting for the viscous dissipation of the moving membrane in a bulk fluid of viscosity η, in the simplest approach the membrane is considered a two-dimensional viscous continuum susceptible of planar viscous flow characterized by an intrinsic surface viscosity μ_m. In analogy with the similar tensor for bulk fluids in Eq. (S1.12), the Oseen tensor of the viscous membrane embedded in a bulk fluid is (6,20):

$$\Lambda_q = \frac{1}{4\eta q + 2\mu_m q^2}, \tag{S2.13a}$$

which can be rewritten as the usual bulk hydrodynamic compliance, with an effective value of the bulk viscosity whose q-dependency is determined by the ratio of the intrinsic membrane friction to the bulk friction, this is:

$$\Lambda_q = \frac{1}{4\eta_{eff}(q) q} \quad with \quad \eta_{eff}(q) = \eta\left(1 + \frac{\mu_m q}{2\eta}\right) \tag{S12.13b}$$

The global effect of membrane viscosity on membrane dynamics is to introduce an effective increase of frictional dissipation at spatial scales smaller than a characteristic length, $L_C \approx \mu_m/2\eta$, below which the intrinsic effects of membrane viscosity become dominant. At large distances ($q << L_C^{-1}$), one expects a regular friction governed by the constant value of the bulk viscosity $\eta_{eff} \approx \eta$. However, at short distances ($q >> L_C^{-1}$), the effective viscosity is expected to increase as $\eta_{eff}(q) \approx \mu_m q$, in a thickening regime governed by the intrinsic membrane viscosity. At $q \approx L_C^{-1}$ the hydrodynamic compliance smoothly crossovers from the regular bulk regime into a new frictional regime dominated by membrane viscosity (see Fig. S3). As far the relaxation rates of the modes are determined by the strength of the hydrodynamic compliance, the above described renormalization implies important consequences on the relaxation dynamics depending on the relevant frictional regime. For the sake of simplicity, we first consider the influence of renormalized friction on the relaxation of the pure bending modes. In this particular case, the relaxation rates are expected to renormalize between two limiting regimes:

$$\omega_q = E_q \Lambda_q = \frac{\kappa}{4\eta_{eff}} q^3 \begin{cases} \omega_q^{(bulk)} \approx \dfrac{\kappa}{4\eta} q^3 \quad at \quad q << L_c^{-1} \\ \omega_q^{(memb)} \approx \dfrac{\kappa}{2\mu_m} q^2 \approx \dfrac{\kappa}{4\eta L_C} q^2 \quad at \quad q >> L_c^{-1} \end{cases} \tag{S2.14}$$

In practice, one expects a dispersive behavior in the relaxation rates, $\omega_q \sim q^{2+\alpha}$ with a dispersion exponent $(2+\alpha)$ that renormalizes as $\alpha = 1$ (bulk regular) $\rightarrow 0$ (membrane). If one looks at the equatorial fluctuations, depending on the value of α, the dynamic correlations of the combined spherical harmonics are expected to vary as:

$$\left\langle h(q,0)h(q,t)\right\rangle_{bend} \approx R^2 \frac{k_B T}{\kappa} \int_q^\infty \frac{\exp\left[-\left(\kappa q^{2+\alpha}/4\eta_{eff}\right)t\right]}{q^4 R^4} R dq \tag{S2.15a}$$

Similarly to the integration performed with Eq. (S2.1), we consider the change of variable:

$$\begin{gathered} \left(\kappa q^{2+\alpha}/4\eta_{eff}\right)t = \omega_q t = z^{2+\alpha} \\ q\left(\kappa t/4\eta_{eff}\right)^{1/(2+\alpha)} = z \end{gathered} \quad \Rightarrow \quad dq = \left(\kappa t/4\eta_{eff}\right)^{-1/(2+\alpha)} dz \tag{S2.16}$$

Then, Eq. (S2.15a) can be rewritten with the simplified form:

$$ACF_{bend}(q,\alpha;t) \approx \frac{1}{R}\frac{k_B T}{\kappa q^3}\left(\omega_q t\right)^{3/(2+\alpha)} \int_z^\infty \frac{\exp\left(-z^{2+\alpha}\right)}{z^4} dz\,, \tag{S2.15b}$$

which equals to Eq. (S2.4) in the case of regular friction ($\alpha = 1$).

The integral kernel in the right side of Eq. (2.15b) can be expressed in terms of the special function Generalized Exponential Integral $E_a(x)$ as:

$$\int_z^\infty \frac{\exp\left(-z^{2+\alpha}\right)}{z^4} dz = -\frac{1}{2+\alpha}\left[\frac{E_{(5+\alpha)/(2+\alpha)}\left(z^{2+\alpha}\right)}{z^3}\right]_z^\infty \tag{S2.16a}$$

with the special function $E_a(x)$ defined as:

$$E_a(x) = \int_1^\infty \frac{e^{-xu}}{u^a} du\,, \tag{S2.17}$$

which takes the limiting value $E_a(\infty) = 0$ in the upper limit of the definite integrate in Eq. (S2.16a), so, one gets:

$$\int_z^\infty \frac{\exp\left(-z^{2+\alpha}\right)}{z^4}dz = \frac{1}{2+\alpha}\frac{\mathrm{E}_{(5+\alpha)/(2+\alpha)}\left(z^{2+\alpha}\right)}{z^3}, \tag{S2.16b}$$

which, using the recurrence relation:

$$a\mathrm{E}_{a+1}(x) = e^{-x} - x\mathrm{E}_a(x) \tag{S2.18}$$

converts to:

$$\int_z^\infty \frac{\exp\left(-z^{2+\alpha}\right)}{z^4}dz = \frac{\exp\left(-z^{2+\alpha}\right) - \left(z^{2+\alpha}\right)\mathrm{E}_{3/(2+\alpha)}\left(z^{2+\alpha}\right)}{3z^3} \tag{S2.16c}$$

Therefore, the *ACF* in Eq. (S2.15b) can be re-written as:

$$ACF_{bend}\left(q,\alpha;t\right) \approx \frac{1}{3R}\frac{k_BT}{\kappa q^3}\left[e^{-\omega_q t} - \left(\omega_q t\right)\mathrm{E}_{3/(2+\alpha)}\left(\omega_q t\right)\right], \tag{S2.15c}$$

which exactly coincides with Eq. (S2.6) in the regular case of bulk friction ($\alpha = 1$).

At the opposite limit of non-regular membrane friction ($\alpha = 0$), one has:

$$ACF_{bend}\left(q,\alpha=0;t\right) \approx \frac{1}{3R}\frac{k_BT}{\kappa q^3}\left[e^{-\omega_q t} - \left(\omega_q t\right)\mathrm{E}_{3/2}\left(\omega_q t\right)\right], \tag{S2.19}$$

which is equivalent to the limiting solution of Eq. (S2.15a) in the hydrodynamic regime where membrane viscosity dominates over bulk viscosity ($\eta_{eff} \approx \mu_m q/2$), this is:

$$\left\langle h\left(q,0\right)h\left(q,t\right)\right\rangle_{bend} \approx R^2\frac{k_BT}{\kappa}\int_q^\infty \frac{\exp\left[-\left(\kappa q^2/2\mu_m\right)t\right]}{q^4R^4}Rdq \tag{S2.15d}$$

In this case, making the appropriate change of variable,

$$\begin{aligned}\left(\kappa q^2/2\mu_m\right)t = \omega_q t = z^2 \\ q\left(\kappa t/2\mu_m\right)^{1/2} = z\end{aligned} \quad \Rightarrow \quad dq = \left(\kappa t/2\mu_m\right)^{-1/2}dz \tag{S2.20}$$

after integration, the expression for the ACF takes the asymptotic form:

$$\begin{aligned}&ACF_{bend}\left(q,\alpha=0;t\right) \approx \\ &\approx \frac{1}{3R}\frac{k_BT}{\kappa q^3}\left\{e^{-\omega_q t}\left(1-2\omega_q t\right) + 2\sqrt{\pi}\left(\omega_q t\right)^{3/2}\,\mathrm{erfc}\left(\sqrt{\omega_q t}\right)\right\}\end{aligned} \tag{S2.21}$$

with the special function erfc(x) defined as:

$$\mathrm{erfc}(x) = \frac{1}{\sqrt{\pi}} \int_z^{\infty} e^{-u^2} du \qquad \text{(S2.22)}$$

The expression in Eq. (S2.21) is analytically equivalent to the more compact formula in Eq. (S2.15c), which can be alternatively implemented in fitting algorithms when a hydrodynamic regime dominated by membrane viscosity is expected. In practice, a continuous crossover between bulk controlled ($\alpha = 1$) and membrane dominated ($\alpha = 0$) relaxation is expected with increasing q, thus, for bending-like modes, the time dependence of the ACF is expected with the generalized profile given by Eq. (S2.15c) as a function of the dispersion parameter α, varying as $\alpha = 1 \rightarrow 0$ as q increases.

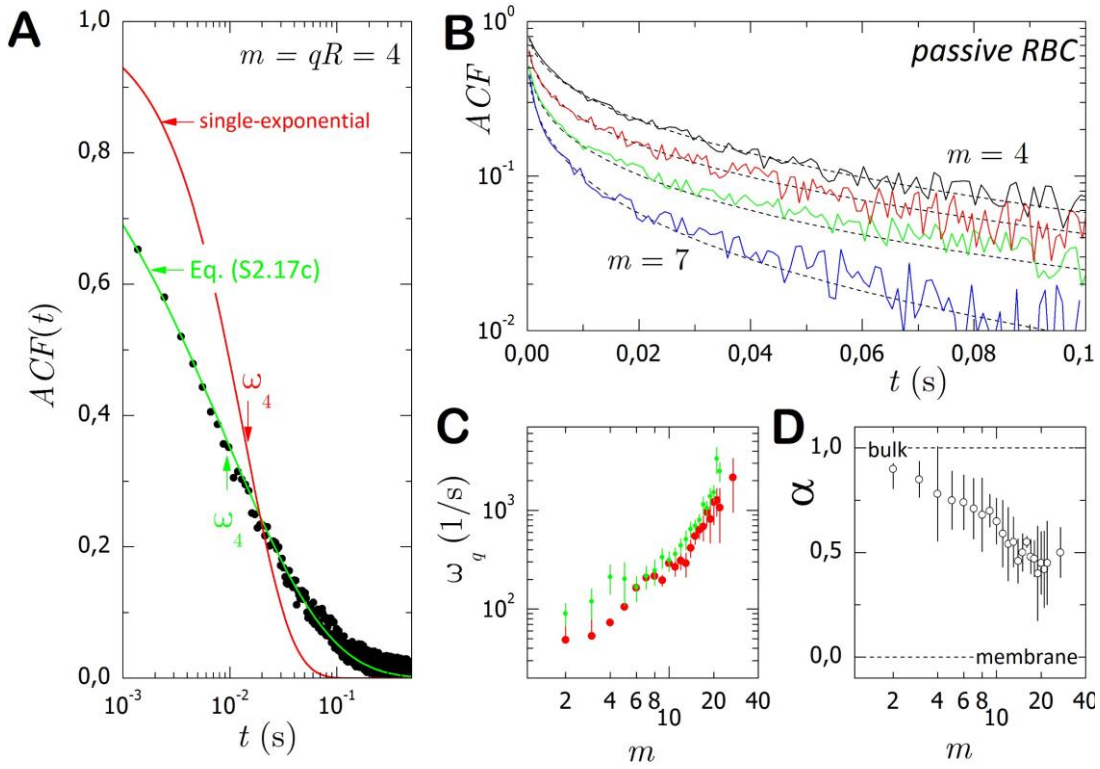

Fig. S4. Experimental autocorrelation function ACF of the passive RBC-flicker. **A)** Typical experimental ACF for m = 4 (symbols) with fits to a single-exponential profile (red) and the exact α–dependent profile in Eq. (S2.17c). The single exponential model is poor in describing the experimental decay and largely overestimates the actual values of the relaxation times (see arrows marking the values of ω_4 obtained from the two models). **B)** Fits of several ACFs of consecutive modes ($m = 4 \rightarrow 7$) to the exact profile in Eq. (S2.17c) (the fitted values of α are plot in D)). **C)** Relaxation rates as obtained from the fits to the single-exponential model (red) and to the exact model in Eq. (S2.17c) (green). Systematically slower rates are obtained with the single-exponential model (red) with respect to the exact decay rates of the experimental profiles (green) obtained from the fits to exact model. **D)** Experimental values of the q-dependent renormalization exponent α describing the effective dispersion of the bending mode $\omega_q \sim q^{2+\alpha}$. As expected a monotonous increase from a bulk-like regime ($\alpha = 1$) down to a membrane-dominated regime is observed with increasing q (α–values from fits in B)).

The results in Figure S4 evidence the adequacy of the α–dependent model to describe the experimental profiles of the ACF of the equatorial thermal modes in the RBC. In particular, Figure S4.A shows a representative ACF for the thermal fluctuations in a drugged RBC ($q = m/R$ with $m = 4$). The experimental relaxation clearly deviates from the single-exponential profile as a stretched-like profile corresponding to a broad distribution of relaxation times rather than to a single relaxation time. The single exponential describe a homogenous relaxation at a rate effectively slower than the phenomenological relaxation rate estimated as an inverse decay time, $\tau^{-1} \approx \omega$ (when $\mathrm{ACF}(t = \tau) = 1/e \approx 0.37$). However, the sum-of-modes function in Eq. (S2.15c) is perfectly able to fit the experimental profiles (see Fig. S4A/B) with relaxation rates higher than those provided by the single-relaxation model (see Fig. S4C) and reasonable values of the dispersion exponent α accounting from effective relaxation between the two limiting frictional regimes, from $\alpha \approx 1$ (bulk friction at low q) down to $\alpha \to 0$ (membrane friction at high q) (see Fig. S4D).

SI3. Power spectral density

The power spectral density (PSD), or simply power spectrum, is a positive real function that measures the frequency content of the stochastic process, this is, how the energy of the signal is distributed with frequency. For a flickering signal $h(t)$, this can be calculated as:

$$PSD(\omega) = \frac{1}{2\pi}\left\| \int_{-\infty}^{\infty} h(t) e^{-i\omega t} dt \right\|^2 \qquad \text{(S3.1)}$$

SI3.a) Experimental determination. In this work, the experimental PSDs were computed from the experimental time series $h(t)$ using Matlab **pwelch** function. The **pwelch** uses the sample rate specified in Hz to compute the PSD and the related frequencies vector in Hz, corresponding to a given temporal trace. The spectral density obtained is calculated in units^2/Hz. Briefly, following the Welch method (21), the algorithm **pwelch** perform the calculation as:

1. The time trace $h(t_i)$ is divided into m overlapping segments (h_k) each with 50% overlap.
2. A Hamming window is applied to each segment h_k
3. An FFT is applied to the windowed data.
4. The (modified) periodogram of each windowed segment is computed $S(e^{i\omega})$
5. The set of modified periodograms is averaged to form the spectrum estimate
6. The resulting spectrum estimate is scaled to compute the power spectral density as $S(e^{i\omega})/fs$ where fs is the sample rate in Hz.

SI3.b) Theoretical model:

Active contribution to the height-height correlation function. We begin with the model of active membranes (12), to calculate the active contribution to the height-height correlation function $ACF_q{}^{(act)}(t)$. This essentially amounts to the inverse Fourier transform of $ACF_q{}^{(act)}(\omega)$ with respect to frequency. In the ideal tensionless state, the function $ACF_q{}^{(act)}(\omega)$ for the direct force mode is (22):

$$ACF_q^{(act)}(\omega) = \langle h(q,\omega)h(-q,\omega)\rangle = n_m p_{on}\left(f_0\Lambda_q\right)^2 \frac{1}{\omega^2+\omega_q^2}\frac{\omega_{act}^{-1}}{1+\left(\omega/\omega_{act}\right)^2} \quad \text{(S3.1)}$$

where n_m is the areal density of motors on the membrane, p_{on} is the probability of a motor to be active at any given time, f_0 is the intrinsic force per motor, Λ_q is the hydrodynamic Oseen tensor for a free membrane, ω_q is the response frequency of the membrane and ω_{act} is the inverse of the mean burst time of each motor. For the curvature-force model f_0 is replaced by $f_0(rq)^2$, where r is the radius of the induced curvature. Fourier transforming we get:

$$\begin{aligned} ACF_q^{(act)}(t) &= \langle h(q,0)h(-q,t)\rangle = \int d\omega \int d\omega' \langle h(q,\omega)h(-q,\omega')\rangle e^{-i\omega t} \\ &= n_m p_{on}\left(f_0\Lambda_q\right)^2 \frac{1}{\left|\omega_{act}{}^2-\omega_q^2\right|}\left(\frac{\omega_{act}}{\omega_q}e^{-\omega_q t}+e^{-\omega_{act}t}\right) \end{aligned} \quad \text{(S3.2)}$$

We see that the active force contributes to the temporal correlations two terms: The first term on the *l.h.s.* of Eq. (S3.2) decays with the membrane natural frequency ω_m, as do the thermal fluctuations (see Eq. (S2.1)). Compared to the thermal fluctuations in Eq. (S1.9), the amplitude of the active correlations with this decay behaviour decreases with increasing wavevector as q^{-11} compared to q^{-4} (for a free membrane and direct force).

This contribution is therefore negligible for all wavevectors where $\omega_q >> \omega_{act}$, which is the case for the current experiments (Fig.1b, right panel). The second contribution in Eq. (S3.2) decays at the natural "frequency" of the motor, ω_{act}. Both contributions diverge when there is a form of resonance, $\omega_q = \omega_{act}$, which does not occur in the red-blood cell case (Fig. 3b; right panel). The divergence in Eq. S3.2 can be eliminated if the time-scale of the active bursts ω_{act} is in fact not completely decoupled from the relaxation modes of the membrane ω_q (which we assumed for simplicity). Such coupling would mean that in fact the resonance-like condition is averted, for example, if long-range (and large-amplitude) slow membrane modes also slow down the rate of active bursts at that wavelength.

Calculation of the height-height PSD. The frequency-dependent power spectral density (PSD) for thermal fluctuations is given by

$$PSD^{(th)} = \left\langle \left| h(\omega) \right|^2 \right\rangle_{th} = \frac{1}{(2\pi)^2} \int \frac{k_B T \Lambda_q}{\omega^2 + \omega_q^2} d^2 q \qquad \text{(S3.3)}$$

The PSD for the direct force model is

$$PSD^{(act)} = \left\langle \left| h(\omega) \right|^2 \right\rangle_{act} = \frac{1}{(2\pi)^2} \int \frac{\left(f_0 \Lambda_q \right)^2}{\omega^2 + \omega_q^2} \frac{p_{on} n_m \omega_{act}^{-1}}{1 + \left(\omega_q / \omega_{act} \right)^2} d^2 q \qquad \text{(S3.4)}$$

We numerically integrate these expressions for the following range of wavevectors: $\pi/L < q < 0.2\text{nm}^{-1}$, where $L = 8\mu\text{m}$ is the lateral size of the RBC membrane. Numerically integrating the PSD for the active component for small−ω, where the tension is dominant, gives the well-behaved function plotted in Fig. 4A.

References

1. Schneider MB, Jenkins JT, Webb WW (1984) Thermal fluctuations of large quasi-spherical bimolecular phospholipid-vesicles. J Phys France, 45:1457-1472.

2. Milner ST, Safran S. (1987) Dynamical fluctuations of droplet microemulsions and vesicles. Phys Rev B 36: 4371-4379

3. Faucon JF, Mitov MD, Méléard P, Bivas I, Bothorel P (1989) Bending elasticity and thermal fluctuations of lipid membranes: Theoretical and experimental requirements. J Phys France 50, 2389-2414

4. Pécreaux J, Dobereiner HG, Prost J, Joanny JF, Bassereau P (2004) Refined contour analysis of giant unilamellar vesicles. Eur Phys J E 13: 277-290

5. Helfrich W (1975) Out-of-plane fluctuations of lipid bilayers. Zeitschrift für Naturforschung. Section C: Biosciences 30: 841.

6. Seifert U and Langer S (1993) Viscous modes of fluid bilayer membranes. EPL (Europhysics Letters) 23: 71.

7. Zilman A and Granek R (1996) Undulations and dynamic structure factor of membranes. Phys Rev Lett 77: 4788-4791.

8. Yoon YZ, Hong H, Brown A, Kim DC, Kang DJ, Lew VL, Cicuta P (2009) Flickering analysis of erythrocyte mechanical properties: dependence of oxigenation, cell shape and hydration level. Biophys J 97: 1606-1615.

9. Deuling H and Helfrich W (1976) Red blood cell shapes as explained on the basis of curvature elasticity. Biophys J 16: 861-868.

10. Waugh R and Evans E (1979) Thermoelasticity of red blood cell membrane. Biophys J 26: 115-131.

11. Lipowsky R, Girardet M (1990) Shape fluctuations of polymerized or solidlike membranes. Phys. Rev. Lett. 65: 2893.

12. Gov N, Zilman AG, Safran S. (2003) Cytoskeleton Confinement and Tension of Red Blood Cell Membranes. Phys Rev Lett 90: 228101-1-4

13. Auth T, Safran SA and Gov NS (2007) Fluctuations of coupled fluid and solid membranes with application to red blood cells. Phys Rev E 76: 051910.

14. Brochard F, Lennon JF (1975) Frequency spectrum of the flicker phenomenon in erythrocytes. J Physique (Paris) 36: 1035-1047.

15. Leibler S, Singh RR, and Fisher ME (1987) Thermodynamic behavior of two-dimensional vesicles. Phys Rev Lett 59:1989-1992.

16. Zeman K, Engelhard H and Sackmann E (1990) Bending undulations and elasticity of the erythrocyte membrane: effects of cell shape and membrane organization. Eur Biophys J 18: 203-219.

17. Huang JS et al. (1987) Study of dynamics of microemulsion droplets by neutron spin-echo spectroscopy. Phys Rev Lett 59: 2600-2603.

18. Hughes BD, Pailthorpe BA, White LR (1981) The translational and rotational drag on a cylinder moving in a membrane. J Fluid Mech 110: 349-372.

19. Lubensky DK and Goldstein RE (1996) Hydrodynamics of monolayer domains at the air–water interface. Phys Fluids 8: 843-854.

20. Camley BA, Brown FLH (2011) Beyond the creeping viscous flow limit for lipid bilayer membranes: Theory of single-particle microrheology, domain flicker spectroscopy, and long-time tails. Phys Rev E 84: 021904

21. Welch P (1967). The use of fast Fourier transform for the estimation of power spectra: a method based on time averaging over short, modified periodograms. Audio and Electroacoustics, IEEE Transactions 15:70-73.

22. Gov NS (2004) Membrane undulations driven by force fluctuations of active proteins. Phys Rev Lett 93: 268104